

NanoSIMS analysis and Auger electron spectroscopy of silicate and oxide stardust from the carbonaceous chondrite Acfer 094

Christian Vollmer^{a,*}, Peter Hoppe^a, Frank J. Stadermann^b,
Christine Floss^b, Frank E. Brenker^c

^a Max Planck Institute for Chemistry, Particle Chemistry Dept., Joh.-J.-Becherweg 27, D-55128 Mainz, Germany

^b Laboratory for Space Sciences and Physics Dept., Washington University, St. Louis, MO 63130, USA

^c Geoscience Institute/Mineralogy, Goethe-University Frankfurt, Altenhoferallee 1, D-60438 Frankfurt, Germany

Received 21 January 2009; accepted in revised form 16 August 2009; available online 23 August 2009

Abstract

We have detected 138 presolar silicate, 20 presolar oxide and three presolar complex grains within the carbonaceous chondrite Acfer 094 by NanoSIMS oxygen isotope mapping. These grains were further investigated by scanning electron microscopy (SEM) and Auger electron spectroscopy for morphological and chemical details and their distribution within the meteorite matrix. The three complex grains consist of Al-rich oxides (grossite and hibonite) attached to non-stoichiometric Si-rich silicates. Refractory Al-rich oxides therefore serve as seed nuclei for silicates to condense onto, which is proposed by condensation theory and astronomical observations. However, in the majority of presolar silicates we did not find any indications for large subgrains. Most of the grains (80%) belong to O isotope Group I (¹⁷O-enriched) and come from 1 to 2.5 M_⊙ asymptotic giant branch (AGB) stars of close-to-solar or slightly lower-than-solar metallicity. About 60% of these grains are irregular in shape; ~40% display elliptical morphologies together with smooth, platy surfaces. Three grains with large ¹⁷O enrichments (¹⁷O/¹⁶O > 3 × 10⁻³) have highly irregular shapes and are very small (<250 nm); these grains may have formed in binary star systems or around higher mass (~3 M_⊙) AGB stars. About 10% of the presolar silicates in this study can be assigned to the O isotope Group IV, which most likely originate from type II supernovae (SNeII). These grains are also generally smaller than 300 nm and are often irregular in shape (88%), consistent with the SNeII origin scenario. The presolar grains are generally evenly distributed within the matrix on an mm scale, although in one case a statistically significant clustering of five grains in one 10 × 10 μm² sized field is observed. This could be an important hint that the distribution of presolar material in the parental molecular cloud was heterogeneous on a very fine scale. The matrix-normalized abundance of silicate stardust in Acfer 094 is 163 ± 14 ppm, which is among the highest abundance of O-rich stardust in primitive meteorites. Oxide stardust comprises 26 ± 6 ppm of the matrix. Auger Nanoprobe measurements of 69 presolar silicates and oxides (30 on a quantitative, 39 on a qualitative basis) indicate that most of the grains are Fe-rich (Mg/(Mg + Fe) of 0.82 and lower), which is either due to non-equilibrium condensation, secondary alteration, or both. (Mg + Fe)/Si ratios of the silicates are mostly non-stoichiometric and scatter around pyroxene-like rather than olivine-like compositions, which is consistent with recent Auger and transmission electron microscopy observations and astrophysical predictions. Mg-rich grains (Mg/(Mg + Fe) > 0.5) more likely exhibit elliptical, smooth surfaces (14 out of 18 grains), which is an indication that these grains have not been strongly altered since their circumstellar condensation. We identified only one grain similar to the “glass with embedded metal and sulfides” (GEMS) with a statistically significant sulfur content (>2–3 at.%). It remains unclear why the typical high-sulfur GEMS grains are only found in interplanetary dust particles, but have not yet been unequivocally identified in primitive meteorites.

© 2009 Elsevier Ltd. All rights reserved.

* Corresponding author. Tel.: +49 6131 305350.

E-mail address: cvollmer@mpch-mainz.mpg.de (C. Vollmer).

1. INTRODUCTION

Circumstellar silicate grains from supernova or nova explosions and red giant stars survived alteration and homogenization processes in the solar nebula and are detected in meteorites and interplanetary dust particles (IDPs) through their highly anomalous isotopic compositions (see, e.g., Hoppe and Vollmer, 2008, for a recent review). These “presolar” fingerprints point to nucleosynthetic reactions in stellar interiors, because they cannot be explained by any process in the solar system. Analysis of this “stardust” allows testing of astrophysical models of stellar evolution and nucleosynthesis, dust condensation in circumstellar environments, dust modification in the interstellar medium (ISM) and galactic chemical evolution (GCE) of the elements. They are also an important tool to investigate the origin and evolution of the nascent solar system.

A classification scheme developed by Nittler et al. (1997) based on O-isotopic compositions of presolar oxides can also be applied to presolar silicates. Group I silicates/oxides exhibit enrichments in ^{17}O and close-to-solar or slightly lower-than-solar $^{18}\text{O}/^{16}\text{O}$ ratios. Most of these grains come from 1 to 2.5 M_{\odot} asymptotic giant branch (AGB) stars as inferred from a comparison of the grain data with astronomical observations (Harris and Lambert, 1984) and theoretical considerations (Boothroyd and Sackmann, 1999). It is possible, though, that some highly ^{17}O -enriched silicates ($^{17}\text{O}/^{16}\text{O} > 3 \times 10^{-3}$) may have originated in binary star systems (Nittler et al., 2008; Vollmer et al., 2008). Group II silicates/oxides display strong depletions in ^{18}O and most of these grains are thought to come from AGB stars with a lower-than-solar metallicity and/or from AGB stars that experienced cool bottom processing (Nollett et al., 2003). Group III grains have ^{16}O excesses and, based on GCE considerations, might come from stars of lower mass and metallicity compared to the parent stars of the other grains. However, GCE interpretations of the O isotopes are still hampered by uncertainties and some of these grains might also have a supernova origin (Nittler, 2007). Group IV grains have moderate to large enhancements in ^{18}O and their isotopic compositions are best-explained by formation in type II supernovae (SNeII) (Nittler et al., 2008; Vollmer et al., 2008).

Mineralogical and chemical analyses of stardust silicates are hampered by the extremely small sizes of the grains (mostly <400 nm) and the possibility of contamination from surrounding solar system silicates. A fraction of stardust silicates have been analyzed by transmission electron microscopy (TEM), but sample preparation by the focused ion beam technique is highly elaborate and only small sets can be analyzed (e.g., Stroud et al., 2008; Vollmer et al., 2009). As a viable alternative, grains can also be measured in situ by Auger electron spectroscopy, where elemental abundances are quantified by comparison with mineral standards (Stadermann et al., 2009). This is a relatively new technique in the cosmochemical field, but, compared to the time-consuming and often risky sectioning of single grains for TEM, larger sample sets can be analyzed without any additional preparation (Nguyen et al., 2007b, 2008b; Bose et al., 2008a; Floss and Stadermann, 2009). It is also

a promising alternative to SEM/EDX analysis, because the spatial resolution is not limited by the excitation volume of the X-rays generated, which is usually larger than the size of the presolar silicates. Auger electrons are extracted from only the top few nanometers of the sample; the spatial resolution of this technique therefore is limited by the resolution of the primary electron beam, and is on the order of 10–20 nm, two orders of magnitude better than EDX. Some rare presolar grain types have already been detected by this technique (Floss et al., 2008). Furthermore, Auger elemental maps can provide important constraints on complex mineral assemblages. Results on chemical compositions and morphological details can be compared to infrared (IR) observations of silicate dust around evolved stars (e.g., Molster et al., 2002a,b,c) and SNI explosions (e.g., Rho et al., 2008). Here we report on investigations of the O-isotopic compositions, morphologies, distribution, abundances and chemical compositions of stardust silicate and oxide grains from the carbonaceous chondrite Acfer 094 by combined NanoSIMS/SEM/Auger Nanoprobe analyses. The O-isotopic compositions of a fraction of these grains have been previously reported by Vollmer et al. (2008).

2. SAMPLES AND EXPERIMENTAL

The Acfer 094 meteorite from the Sahara desert is one of the most pristine samples of the nascent solar system available for cosmochemical studies. Extensive characterization of this ungrouped carbonaceous chondrite has revealed an unusually low degree of thermal and aqueous alteration (Greshake, 1997), although there appear to be some minor terrestrial weathering effects (Alexander et al., 2007; Bland et al., 2008). It also contains high amounts of presolar material like SiC and silicates in the 50–150 ppm range and, thus, represents a valuable reservoir to study early solar system evolution and stardust samples (e.g., Newton et al., 1995).

We chose fine-grained matrix areas in a polished thin section of Acfer 094 for isotopic mapping with the NanoSIMS at the Max Planck Institute (MPI) for Chemistry. A focused Cs^+ ion beam (beam diameter ~ 100 nm, primary current ~ 1 pA) was rastered over a large number of subareas, each $10 \times 10 \mu\text{m}^2$ in size, and negative secondary ions of $^{16,17,18}\text{O}$, ^{28}Si and $^{27}\text{Al}^{16}\text{O}$ were simultaneously detected and converted to 256^2 pixel images. The matrix areas were previously sputtered using a high beam current (~ 10 pA) to remove the carbon coating on $14 \times 14 \mu\text{m}^2$ large fields and to implant Cs. Total integration time for each ion image was ~ 1 h, resulting in a relative counting statistical error for the $^{17}\text{O}/^{16}\text{O}$ ratio of less than 10% in a typical 300 nm sized grain. The measurements were performed in automatic mapping mode, where the stage moves from one field to the next in a pre-defined raster. A total area of $70,500 \mu\text{m}^2$ (705 fields) was scanned in this way. All grains with O-isotopic anomalies $>4\sigma$ away from the isotopically normal background in at least one isotope ratio were considered presolar. Only the innermost 4×4 pixel (~ 160 nm) regions of interest of the grain were chosen for data reduction in most cases,

whereas larger regions were integrated over some grains of larger dimensions. The distinction between silicates and Al-rich oxides was based on ^{28}Si and $^{27}\text{Al}^{16}\text{O}$ ion images compared to the surrounding matrix, except for grains with acquired Auger data. Measurements were done with mass resolutions of $m/\Delta m = 2500$ (^{16}O , ^{18}O) and 4500 (^{17}O), sufficient to separate the isobaric interference ^{16}OH from ^{17}O . Identified grains were subsequently relocated, documented and imaged in the field emission (FE)-SEM by secondary electron detection.

Auger analyses of the grains were carried out with the PHI 700™ Scanning Auger Nanoprobe at Washington University in St. Louis (USA). Prior to the analyses, a 2 kV/1 μA Ar^+ ion beam was scanned over a broad 2 mm area of the sample surface to remove atmospheric contamination. In a first set of grains, several point measurements were performed at 10 kV and 1–10 nA for about 10 min per grain. In a second set of grains, the electron beam was rastered over the grains of interest for about 30 min at 10 kV/0.3 nA. The acquired energy spectra from 30 to 1730 eV were then differentiated using a 7-point smoothing and Savitsky–Golay differentiation routine prior to peak identification (Stadermann et al., 2009). Because measurement conditions changed between the first and second set of analyses and sensitivity factors for silicate minerals were obtained under measurement conditions similar to the second set of analyses (Stadermann et al., 2009), quantitative results are available only for the latter (30 grains). Since Auger electron spectroscopy is a surface analytical technique, the measured compositions reflect the makeup of the top few nanometers directly under the electron beam. Extensive tests have shown that there is no difference in composition between sputtered and unsputtered grains within the analytical errors, which eliminates any influence on the compositions from the preceding NanoSIMS measurements (Stadermann et al., 2009). By comparison with olivine and pyroxene reference standards, elemental compositions can be determined from the differentiated peaks using experimentally derived sensitivity factors for O (0.194), Si (0.121), Mg (0.234), Fe (0.150), Ca (0.626) and Al (0.160). The reported 1σ uncertainties of elemental contents and ratios have been obtained from the relative uncertainties of the sensitivity factors, which are O, 3.6%; Si, 11.0%; Mg, 9.4%; Fe, 11.2%; Ca, 10.8%; and Al, 24.9%. The high uncertainty for Al is due to its relatively low sensitivity in the Auger Nanoprobe. Other non-systematic errors such as sample charging or the presence of residual surface contamination may also affect these uncertainties, which are thus likely to be lower limits. Analyses on different samples indicate that relative Auger sensitivity factors for oxides and silicates are the same within errors. Auger elemental distribution maps were usually acquired with ~ 5 nA beam current, where the electron beam scanned over about 2×2 to $5 \times 5 \mu\text{m}^2$ large areas around the grains of interest and acquired Auger signals were converted into digitized 256² pixel images for previously defined element peaks. These maps cannot be quantified, but provide important information on the spatial distribution of measured elements and, therefore, different phases.

3. RESULTS

3.1. Oxygen isotopes

A total of 141 presolar silicates together with 20 Al-rich presolar oxides were detected within 705 analyzed fields of $100 \mu\text{m}^2$ each. Three of the 141 presolar silicate grains contain Al-rich subgrains larger than 200 nm, which will be discussed later in more detail (Sections 3.4.2 and 4.4.2). Oxygen isotopic data, Auger results and morphological details of the silicate and oxide grains are compiled in Tables 1–3. The vast majority (131 grains) of presolar silicates and oxides are from Group I ($81 \pm 7\%$ of all grains, $81 \pm 8\%$ of the silicate grains, 1σ errors derive from Poisson statistics throughout this work). $^{17}\text{O}/^{16}\text{O}$ ratios of the majority of Group I grains range from 4.48×10^{-4} to 2.20×10^{-3} with an arithmetic mean at 8×10^{-4} ; $^{18}\text{O}/^{16}\text{O}$ ratios span the range 1.19 – 2.26×10^{-3} (Fig. 1; solar values (standard mean ocean water (SMOW): $^{17}\text{O}/^{16}\text{O} = 3.83 \times 10^{-4}$, $^{18}\text{O}/^{16}\text{O} = 2.01 \times 10^{-3}$). Seven silicates, three Al-rich oxides and one complex grain (22_09) belong to the ^{18}O -depleted Group II ($^{18}\text{O}/^{16}\text{O} < \sim 1 \times 10^{-3}$), which represents $7 \pm 2\%$ of the whole O-rich stardust population in this study. $^{18}\text{O}/^{16}\text{O}$ ratios of these grains range from 5.97 to 10.5×10^{-4} , $^{17}\text{O}/^{16}\text{O}$ ratios from 5.38 to 10.2×10^{-4} . Group III grains comprise by far the smallest group of all detected O-rich stardust grains and make up only 2% of the O-rich stardust population in this study. All three Group III grains are silicates and have $^{17}\text{O}/^{16}\text{O}$ ratios from 1.91 to 2.27×10^{-4} and close-to-normal $^{18}\text{O}/^{16}\text{O}$. Group IV grains are all silicates and their $^{18}\text{O}/^{16}\text{O}$ ratios range from 2.35 to 3.36×10^{-3} with close-to-normal $^{17}\text{O}/^{16}\text{O}$ values. The 16 grains comprise $10 \pm 3\%$ of the O-rich stardust population from this study ($11 \pm 3\%$ of the presolar silicate population).

3.2. Grain shapes

Documentation by FE-SEM was possible for 120 out of 141 presolar silicates; the remaining 21 grains were characterized by the shape of the O anomaly in the NanoSIMS ion image. Most of the grains ($\sim 60\%$) are irregular in shape, i.e., not elongated, isometric or needle-like, while about 40% display elliptical or circular shapes (Tables 1–3). A few of these exhibit an isometric shape and may be elongated grains viewed along the major axis. In the presolar oxide population, about half of the grains are circular or elliptical, the rest exhibit irregular outlines. There is an apparent distinction between smooth/platy grain surfaces, which stick out of the surrounding matrix after the NanoSIMS analyses and thus appear brighter in the SE images, and irregular/polyaggregate grains that seem to consist of smaller particles (Fig. 2). Irregular grains are harder to locate within the matrix, which mainly consists of amorphous silicates of comparable appearance. A few grains (e.g., 26_06, 31_09b, Figs. 2 and 3) exhibit tiny cracks and fissures. This appearance is different from the polyaggregate morphology mentioned above. The three Group III grains could not be relocated in the SEM at all. Group

Table 1

Oxygen isotope ratios, sizes and morphologies of presolar silicates (bold-typed) and oxides from Acfer 094 without Auger data. Oxygen isotope data of grains in *cursive* are already published in Vollmer et al. (2008). Reported errors are 1σ .

Grain	Group ^a	Size (nm) (SEM)	Morphology	¹⁷ O/ ¹⁶ O ($\times 10^{-4}$)	¹⁸ O/ ¹⁶ O ($\times 10^{-3}$)
Chr2_1_2a	I	280 × 130	Elliptical	8.84 ± 0.51	2.23 ± 0.08
Chr2_1_2b	I	280 × 200	Elliptical	6.02 ± 0.37	1.30 ± 0.05
Chr2_1_6	I	280 × 230	Isometric	8.38 ± 0.39	1.84 ± 0.05
Chr2_1_7	I	440 × 420	Irregular	7.36 ± 0.38	1.49 ± 0.05
Chr2_1_8	I	280	Isometric	5.98 ± 0.32	2.06 ± 0.06
Chr3_1_8	I	280*	Isometric	5.79 ± 0.36	1.81 ± 0.06
Chr3_1_10	I	360 × 170	Elliptical	6.42 ± 0.42	2.07 ± 0.07
<i>1_15b</i>	I	300	Irregular	6.75 ± 0.75	2.15 ± 0.13
4_23	I	230	Irregular	7.09 ± 0.54	2.09 ± 0.09
6_06	I	340 × 180	Irregular	7.26 ± 0.57	2.02 ± 0.10
6_09	I	350 × 300	Irregular	9.87 ± 0.47	1.90 ± 0.06
7_03b	I	160	Irregular	7.07 ± 0.48	2.09 ± 0.08
7_04^b	I	1000 × 600 (core: 500 × 350)	Elliptical (core: triangular)	5.74 ± 0.15	1.30 ± 0.02
7_12	I	310 × 200*	Irregular	6.74 ± 0.61	1.42 ± 0.09
7_15a	I	230	Isometric	7.54 ± 0.61	2.05 ± 0.10
8_05	I	330	Irregular	8.92 ± 0.71	1.85 ± 0.10
8_10	I	810 × 490	Elliptical	8.07 ± 0.37	1.77 ± 0.05
8_12	I	470 × 370	Elliptical	10.21 ± 0.73	1.85 ± 0.09
9_15	I	300 × 270*	Irregular	5.53 ± 0.36	1.58 ± 0.06
10_03	I	300	Irregular	6.96 ± 0.50	1.66 ± 0.08
10_06	I	340 × 250	Irregular	7.60 ± 0.55	2.22 ± 0.09
11_07	I	450 × 150	Elliptical	15.82 ± 0.63	2.00 ± 0.07
11_10	I	450 × 400	Irregular	10.35 ± 0.72	1.98 ± 0.10
15_2_4	I	400 × 270	Isometric	12.58 ± 0.79	1.91 ± 0.10
15_2_9	I	650 × 300	Irregular	6.22 ± 0.53	1.40 ± 0.08
17_02	I	300	Isometric	6.24 ± 0.30	1.67 ± 0.05
18_08	I	480 × 420	Isometric	8.04 ± 0.51	1.93 ± 0.08
19_04a	I	380 × 350*	Irregular	7.10 ± 0.58	1.89 ± 0.09
19_09	I	350 × 310	Elliptical	8.69 ± 1.00	1.92 ± 0.14
20_08	I	380 × 340	Irregular	6.20 ± 0.42	1.98 ± 0.07
20_13	I	300	Irregular	6.92 ± 0.55	1.95 ± 0.09
22_03	I	300	Irregular	4.48 ± 0.49	1.25 ± 0.08
22_10a	I	450 × 250	Elliptical	8.34 ± 0.68	1.31 ± 0.08
22_12	I	300 × 280	Irregular	6.98 ± 0.49	2.12 ± 0.08
23_02	I	300 × 210*	Irregular	6.78 ± 0.45	1.98 ± 0.07
23_12b	I	330 × 320	Irregular	8.86 ± 0.54	1.91 ± 0.08
24_09	I	180 × 140*	Irregular	6.40 ± 0.44	1.92 ± 0.08
24_10	I	270 × 200	Irregular	7.01 ± 0.58	2.09 ± 0.10
24_19	I	150*	Irregular	5.86 ± 0.44	2.01 ± 0.08
26_10b	I	190	Elliptical	6.84 ± 0.41	2.00 ± 0.07
26_10c	I	270 × 240	Elliptical	9.78 ± 0.45	2.09 ± 0.06
26_10d	I	180*	Irregular	5.76 ± 0.34	2.08 ± 0.06
26_10e	I	180 × 60*	Irregular	5.87 ± 0.38	1.91 ± 0.07
27_13	I	300 × 230	Irregular	5.66 ± 0.43	2.04 ± 0.08
27_14	I	310 × 260	Irregular	8.68 ± 0.70	1.18 ± 0.08
27_16	I	270 × 180	Irregular	5.90 ± 0.39	1.71 ± 0.06
28_07	I	270 × 200	Irregular	8.39 ± 0.62	1.89 ± 0.09
29_03	I	270 × 180	Irregular	7.23 ± 0.42	1.80 ± 0.06
29_12a	I	360 × 260*	Irregular	5.89 ± 0.36	1.88 ± 0.06
29_12b	I	280 × 230	Irregular	6.71 ± 0.40	1.74 ± 0.06
29_14	I	220 × 200	Irregular	5.78 ± 0.36	1.99 ± 0.06
30_01	I	340 × 300	Irregular	5.37 ± 0.36	1.48 ± 0.06
30_14a	I	370 × 280	Irregular	5.98 ± 0.46	1.58 ± 0.07
31_02	I	280 × 170	Irregular	6.75 ± 0.43	1.88 ± 0.07
31_04	I	350	Irregular	8.25 ± 0.39	1.89 ± 0.06
31_05	I	280 × 180*	Irregular	5.05 ± 0.37	1.59 ± 0.06
31_08a	I	370 × 340	Irregular	5.41 ± 0.29	1.75 ± 0.05
31_08b	I	350*	Elliptical	4.88 ± 0.30	1.73 ± 0.05
33_11	I	450 × 350	Irregular	22.02 ± 0.85	1.92 ± 0.08
34_04	I	270*	Isometric	5.09 ± 0.28	2.03 ± 0.06

Table 1 (continued)

Grain	Group ^a	Size (nm) (SEM)	Morphology	¹⁷ O/ ¹⁶ O ($\times 10^{-4}$)	¹⁸ O/ ¹⁶ O ($\times 10^{-3}$)
35_01	I	250 × 230	Irregular	6.00 ± 0.39	2.00 ± 0.07
35_08	I	240 × 170	Elliptical	6.76 ± 0.54	1.92 ± 0.09
Chr2_2_1	II	440 × 410	Isometric	5.48 ± 0.51	0.96 ± 0.06
4_11	II	370 × 230	Elliptical	7.60 ± 0.54	0.92 ± 0.06
7_03a	II	400 × 390	Triangular	8.73 ± 0.65	1.03 ± 0.07
1_08	III	200 [*]	Isometric	1.91 ± 0.38	2.22 ± 0.13
1_12	III	290 × 220 [*]	Isometric	2.01 ± 0.40	2.07 ± 0.13
8_13	III	350 × 190 [*]	Elliptical	2.27 ± 0.31	1.95 ± 0.08
Chr1_1_2	IV	280 × 170	Irregular	4.71 ± 0.28	2.36 ± 0.06
7_15b	IV	250	Irregular	3.91 ± 0.42	2.47 ± 0.10
11_05	IV	200 × 150 [*]	Irregular	3.96 ± 0.34	2.67 ± 0.09
19_2_1a	IV	330 × 290 [*]	Irregular	4.18 ± 0.57	2.82 ± 0.14
20_11a	IV	350 × 180	Irregular	4.22 ± 0.43	2.49 ± 0.10
20_11b	IV	280 × 380 [*]	Irregular	3.73 ± 0.36	2.64 ± 0.09
22_10b	IV	310 × 220	Irregular	4.51 ± 0.51	2.88 ± 0.13
24_17	IV	380 × 300 [*]	Irregular	4.15 ± 0.34	3.35 ± 0.10
30_14b	IV	180 [*]	Elliptical	4.09 ± 0.31	2.47 ± 0.07
32_11	IV	340 × 170 [*]	Elliptical	4.69 ± 0.30	2.37 ± 0.07
33_12	IV	220 × 200	Irregular	3.39 ± 0.33	2.35 ± 0.09
1_15c	I	310 × 290 [*]	Irregular	6.44 ± 0.71	1.76 ± 0.11
2_11	I	300 × 190	Elliptical	8.93 ± 0.91	2.04 ± 0.13
4_28	I	310 × 210	Elliptical	8.17 ± 0.68	1.90 ± 0.10
5_01	I	400	Irregular	16.10 ± 0.75	1.94 ± 0.08
7_06	I	320 [*]	Elliptical	7.24 ± 0.53	1.80 ± 0.08
Chr1_2_15	I	280	Elliptical	13.13 ± 0.47	2.07 ± 0.05
Chr3_1_14	I	270 × 220	Irregular	7.03 ± 0.42	1.48 ± 0.06
11_14	I	330 × 280	Elliptical	5.93 ± 0.42	1.85 ± 0.07
16_03	I	340 × 260	Irregular	7.23 ± 0.60	1.98 ± 0.10
28_05	I	120 [*]	Irregular	5.63 ± 0.37	1.98 ± 0.07
28_10	I	250	Irregular	6.91 ± 0.41	1.93 ± 0.07
29_04	I	370 × 280 [*]	Irregular	6.70 ± 0.48	1.92 ± 0.08
31_03	I	350 × 300 [*]	Irregular	6.23 ± 0.41	1.59 ± 0.06
Solar (SMOW)				3.83	2.01

^{*} Grain size and morphology determined from the NanoSIMS ion image.

^a Group classification according to Nittler et al. (1997) (also applies to subsequent tables).

^b Complex grain consisting of an Al-rich core and a silicate mantle.

IV grains are generally smaller (<300 nm) than the majority of Group I/II grains and also predominantly display irregular morphologies (14 out of 16 grains). Finally, the “extreme” Group I silicates (¹⁷O/¹⁶O > 3 × 10⁻³) were particularly difficult to locate within the matrix, because they are smaller than 250 nm and exhibit highly irregular morphologies (Fig. 4).

3.3. Abundance and spatial distribution

The 141 presolar silicates in 705 analyzed fields yield a total area of 11.49 μm² for a matrix-normalized abundance of 163 ± 14 ppm of silicate stardust in Acfer 094. Twenty-three Al-rich presolar oxide grains were also found and documented by FE-SEM (including the three Al-rich grains in the “complex” presolar silicates), resulting in an abundance of 26 ± 6 ppm. Grain sizes (maximum widths and lengths) were mainly determined from the SE images. Only in cases where the grain had already been sputtered away and/or could not be relocated, were the sizes of the grains determined from the NanoSIMS ion images. This occurred for 21 grains, and in these cases the estimated

grain sizes are probably larger than their real sizes due to overlap of the primary ion beam, whose intensity profile follows a Gaussian distribution, with surrounding isotopically normal material. Grain areas were calculated as ellipses, but as many grains exhibit irregular morphologies, a precise measurement was difficult in these cases. If we recalculate their cross-sectional areas as circles, the arithmetic average diameter of all presolar silicates is 307 ± 8 nm, and that of the Al-rich oxides is 308 ± 19 nm, including the Al-rich subgrains from the three complex grains (Fig. 5). The median size of both presolar oxides and silicates is 300 nm.

Determinations of the absolute area fraction of stardust in a fine-grained matrix are hampered by non-systematic uncertainties, which are discussed by Nguyen et al. (2007b). These authors calculate a detection efficiency for presolar grains, based on the fact that the smallest grains (<~150 nm), cannot be reliably detected in the NanoSIMS. Nguyen et al. (2007b) estimate that their calculated presolar silicate abundance would increase by a factor of ~4 if this detection efficiency is taken into account. The results reported here are not, however, corrected for this

Table 2

Oxygen isotope ratios, sizes, morphologies and qualitative Auger results of presolar silicates (bold-typed) and oxides from Acfer 094. O isotope data of grains in *course* are already published in Vollmer et al. (2008). Auger results in parentheses indicate noisy spectra and, thus, less certain determinations. Reported errors are 1σ .

Grain	Group	Size (nm) (SEM)	Morphology	$^{17}\text{O}/^{16}\text{O}$ ($\times 10^{-4}$)	$^{18}\text{O}/^{16}\text{O}$ ($\times 10^{-3}$)	Auger result
13_01	I	310 × 170	Elliptical	6.60 ± 0.43	1.99 ± 0.07	Fe > Mg
13_04	I	450 × 380	Irregular	20.69 ± 0.80	1.68 ± 0.07	(Fe > Mg)
13_09b	I	240 × 110	Elliptical	5.85 ± 0.32	1.78 ± 0.05	Fe > Mg, Ca
13_11	I	320 × 180	Irregular	6.33 ± 0.43	1.70 ± 0.07	Si, low Mg + Fe
13_13^a	I	300 × 200	Irregular	35.53 ± 0.96	2.07 ± 0.07	Mg > Fe
13_15	I	320 × 280	Isometric	6.31 ± 0.40	1.55 ± 0.06	Fe > Mg
13_16^a	I	350 × 220	Irregular	31.67 ± 0.96	1.97 ± 0.07	Mg > Fe
13_23	I	350 × 310	Elliptical	6.87 ± 0.36	1.45 ± 0.05	Mg ~ Fe, Ca
14_03	I	280	Irregular	7.59 ± 0.44	1.70 ± 0.06	Fe > Mg, Ca
14_11	I	300 × 320	Elliptical	6.37 ± 0.46	1.40 ± 0.07	Mg > Fe, Ca
14_2_1	I	350 × 270	Irregular	6.02 ± 0.43	1.65 ± 0.07	Si, low Mg + Fe
14_2_3a	I	470 × 340	Irregular	8.22 ± 0.43	1.36 ± 0.05	(Si, Ca, Al, low Mg + Fe)
14_2_3b	I	400 × 290	Irregular	12.49 ± 0.49	1.82 ± 0.06	(Mg > Fe)
14_2_5	I	370 × 270	Irregular	5.84 ± 0.41	1.42 ± 0.06	(Si only, Fe)
18_14	I	400 × 280	Irregular	8.43 ± 0.77	2.08 ± 0.12	Mg ~ Fe
21_06	I	570 × 360	Triangular	15.44 ± 0.80	1.94 ± 0.09	Mg > Fe
21_09	I	380 × 360	Irregular	7.47 ± 0.56	1.42 ± 0.08	Fe > Mg, Ca, Al
21_13a	I	380	Irregular	16.17 ± 0.71	2.00 ± 0.08	Fe > Mg, Ca
21_13b	I	300	Irregular	7.15 ± 0.44	1.81 ± 0.07	Mg > Fe
22_02	I	380 × 340	Irregular	7.62 ± 0.67	1.79 ± 0.10	(Mg ~ Fe)
22_23	I	300 × 250	Irregular	9.26 ± 0.62	2.26 ± 0.10	Fe > Mg, Al
23_05	I	400 × 300	Irregular	19.12 ± 0.80	1.82 ± 0.08	(Si, low Mg)
23_06	I	400 × 330	Irregular	7.58 ± 0.51	1.34 ± 0.07	Fe > Mg
23_12a	I	400 × 310	Irregular	13.22 ± 0.63	2.04 ± 0.08	Mg > Fe
23_15^a	I	390 × 240	Irregular	38.49 ± 1.06	2.04 ± 0.08	Mg ~ Fe
24_04	I	250	Irregular	5.93 ± 0.41	2.03 ± 0.07	Fe > Mg, Ca, S
24_08	I	340 × 220	Irregular	6.89 ± 0.41	1.92 ± 0.07	Fe > Mg
25_03	I	380 × 360	Isometric	11.01 ± 0.59	1.98 ± 0.08	Fe > Mg
25_17	I	240 × 200	Irregular	6.07 ± 0.56	1.34 ± 0.08	Mg ~ Fe
14_01	II	420 × 340	Irregular	9.08 ± 0.53	1.01 ± 0.05	Fe > Mg, Ca
22_05	II	530 × 480	Isometric	10.20 ± 0.61	0.78 ± 0.05	Mg > Fe
25_20	II	350 × 310	Isometric	8.22 ± 0.61	0.75 ± 0.06	Mg > Fe
14_09	IV	250 × 200	Irregular	4.07 ± 0.39	2.61 ± 0.10	Mg > Fe
22_10c	IV	460 × 260	Irregular	3.44 ± 0.34	2.99 ± 0.10	Fe > Mg
25_22	IV	330 × 290	Irregular	3.41 ± 0.35	3.36 ± 0.11	Fe > Mg
13_09a	I	200 × 100	Elliptical	5.89 ± 0.32	1.73 ± 0.05	(Al-rich): corundum-like
13_24	I	320 × 270	Irregular	6.60 ± 0.37	1.30 ± 0.05	(Al-rich, Mg): spinel-like
19_04b	I	450 × 370	Isometric	6.17 ± 0.57	1.72 ± 0.09	(Al-rich): corundum-like
19_2_1b	II	850 × 280	Elliptical	8.48 ± 1.02	1.00 ± 0.11	(Al-rich, Ca): hibonite-like

^a “Extreme” Group I grains ($^{17}\text{O}/^{16}\text{O} > 3 \times 10^{-3}$) as defined in Vollmer et al. (2008).

detection efficiency, and we compare our results only with uncorrected values from other NanoSIMS studies. Such comparisons are valid since all NanoSIMS imaging searches can reasonably be assumed to have similar detection efficiencies. Another uncertainty is the precise measurement of the cross-sectional dimensions of the grains, because the boundary between a grain of interest and the surrounding matrix is often equivocal, especially with the majority of grains being irregular in shape. We assume that this uncertainty gets less important with increasing grain numbers, because over- and under-measuring the dimensions of the grains will remove this uncertainty on average. Moreover, grains are not perfect ellipses, but might be closer to a rectangle, adding another source of non-systematic uncertainty. Our reported error based on

counting statistics is therefore only a lower limit to the true uncertainty.

Most of the grains appear to be randomly distributed in the matrix, and there is no abundance gradient observed between matrix and larger components such as chondrules and Ca–Al-rich inclusions. However, some matrix areas are more enriched with presolar material than others, and observed abundances vary between <50 ppm and >200 ppm in different $\sim 100 \times 100 \mu\text{m}^2$ areas. In 17 out of 705 fields analyzed we found a clustering of presolar grains within the matrix on a very small scale, i.e., two or more grains within the same analyzed $10 \times 10 \mu\text{m}^2$ field and even one field containing five presolar silicates (Fig. 6). However, the stardust grains appear evenly distributed on an mm scale.

Table 3a

Oxygen isotope ratios (1σ errors), sizes and morphologies of presolar silicates (bold-typed) and oxides from Acfer 094 (including two complex grains) with quantitative Auger data.

Grain	Group	Size (nm) (SEM)	Morphology	$^{17}\text{O}/^{16}\text{O}$ ($\times 10^{-4}$)	$^{18}\text{O}/^{16}\text{O}$ ($\times 10^{-3}$)
12_02	I	400 \times 380	Irregular	7.36 \pm 0.72	1.61 \pm 0.07
16_08	I	390 \times 200	Elliptical	7.41 \pm 0.70	1.49 \pm 0.10
16_14	I	320	Irregular	7.86 \pm 0.55	1.92 \pm 0.08
26_06	I	590 \times 350	Elliptical	21.12 \pm 0.80	1.63 \pm 0.07
26_10a	I	380 \times 200	Elliptical	9.67 \pm 0.49	1.81 \pm 0.07
26_11	I	280	Irregular	6.11 \pm 0.36	1.68 \pm 0.06
26_12	I	300 \times 250	Isometric	6.32 \pm 0.40	1.93 \pm 0.07
27_02	I	340 \times 220	Elliptical	6.23 \pm 0.50	2.05 \pm 0.08
27_06	I	610 \times 570	Elliptical	7.89 \pm 0.65	1.96 \pm 0.10
27_07	I	320	Irregular	6.12 \pm 0.42	1.64 \pm 0.07
27_09	I	350 \times 190	Elliptical	5.62 \pm 0.33	1.97 \pm 0.06
30_12	I	340 \times 220	Elliptical	5.14 \pm 0.31	1.67 \pm 0.05
30_23	I	500 \times 270	Elliptical	10.53 \pm 0.63	1.74 \pm 0.08
31_09a	I	510 \times 310	Irregular	9.66 \pm 0.54	2.04 \pm 0.08
31_09b	I	480 \times 350	Elliptical	7.84 \pm 0.52	1.73 \pm 0.07
31_09c	I	300 \times 240	Elliptical	4.84 \pm 0.38	1.55 \pm 0.07
31_16	I	420 \times 350	Irregular	6.78 \pm 0.46	1.94 \pm 0.07
32_03	I	600 \times 500 (core: 300 \times 250)	Elliptical (core: irregular)	10.16 \pm 0.49	1.79 \pm 0.06
32_08	I	400	Elliptical	9.26 \pm 0.59	1.95 \pm 0.08
32_13	I	650 \times 530	Elliptical	15.67 \pm 0.69	2.04 \pm 0.08
33_13	I	300 \times 150	Elliptical	6.62 \pm 0.48	2.07 \pm 0.08
34_15	I	370 \times 210	Elliptical	5.88 \pm 0.43	1.44 \pm 0.07
35_19	I	340	Elliptical	6.04 \pm 0.35	1.59 \pm 0.06
31_13	II	670 \times 230	Elliptical	5.38 \pm 0.34	0.93 \pm 0.05
22_09	II	670 \times 480 (core: 340 \times 200)	Elliptical (core: triangular)	8.63 \pm 0.63	0.79 \pm 0.06
33_19	IV	290 \times 210	Irregular	4.04 \pm 0.38	2.66 \pm 0.10
35_11	IV	280	Irregular	4.31 \pm 0.44	3.00 \pm 0.11
27_05	II	530 \times 400	Irregular	8.39 \pm 0.64	1.05 \pm 0.07
28_01	II	540 \times 330	Elliptical	9.67 \pm 0.51	0.60 \pm 0.04
35_17	I	300 \times 250	Isometric	7.99 \pm 0.41	1.93 \pm 0.06

3.4. Auger spectroscopy results

3.4.1. Single grains

We analyzed 60 presolar silicates, seven presolar oxides and two presolar complex grains (Section 3.4.2) by Auger electron spectroscopy. The Auger data of 30 grains could be quantified, whereas the spectra of the remaining 39 grains could only be evaluated qualitatively. Here we mostly focus on the quantitative part of the data. The (Mg + Fe)/Si ratios of the majority of grains scatter around pyroxene-like compositions and show a large spread in values (Fig. 7). About half of the silicates have Mg# (Mg#: Mg/(Mg + Fe)) of 0.5 or lower, or exhibit qualitatively low Mg/Fe ratios in the unquantified data set (47%). The maximum Mg# of the quantified data set is 0.82, excluding one peculiar highly Mg-enriched grain (32_08). No refractory Fe-free silicates were found. The presolar silicates (as well as solar system silicates in the matrix) are often surrounded by tiny (<10 nm) Fe-rich grains (mostly oxides and metal), which appear brighter in the SEM. In one grain documented by Auger analyses, the Fe oxide/metal is located in the center of the presolar grain (grain 27_06, Fig. 3a). Because these observations were made after NanoSIMS measurements that removed some material from the surface of the grain, we conclude that the Fe-material was

located inside the grain and not lying on top of it; however, we note that this conclusion assumes similar sputtering rates for the different materials in the NanoSIMS. The Fe-rich material also seems to be connected to veins of similar appearance that extend to the edge of the presolar grain. If these grains are Fe oxides of solar system origin, then the O isotope anomalies of the presolar grains might be diluted to some extent.

Thirteen grains in the quantified data set display major elemental contents not compatible with either olivine or pyroxene: 10 grains are Si-enriched ((Mg + Fe)/Si < 0.7) and one is Mg-enriched (Mg/Si = 3.4, with Al and Fe < 5 at.%). Two other grains also have very high (Mg + Fe)/Si ratios of 2.8 and 2.4, respectively (27_02 and 33_13, Table 3b and Fig. 7), but examination of the SE images of these grains shows that secondary Fe-rich material has clearly shifted measured values. One silicate (24_04) contains sulfur above the detection limit (2–3 at.%) and may be related to the “glass with embedded metal and sulfides” (GEMS) grains typically found in IDPs (Bradley, 2003). The majority of grains, however, do not exhibit resolvable sulfur peaks, although sulfur is very sensitive in the Auger Nanoprobe.

In the presolar oxide population, grains are dominated by Al and have trace amounts of mostly Ca (Tables 3a

Table 3b

Major element concentrations (at.%, 1σ errors) of presolar silicates (bold-typed) and oxides in Acfer 094 (including two complex grains).

Grain	O	Si	Mg	Fe	Ca ^a	Al	Cation/O	Mg/(Mg + Fe) (=Mg#)	(Mg + Fe)/Si	Phase
12_02	57.1 ± 2.1	21.7 ± 2.4	6.2 ± 0.6	13.6 ± 1.5	1.5 ± 0.2		0.75 ± 0.06	0.31 ± 0.04	0.9 ± 0.1	Pyroxene
16_08	62 ± 2.2	22.5 ± 2.5	8.3 ± 0.8	7.2 ± 0.8			0.61 ± 0.05	0.54 ± 0.06	0.7 ± 0.1	Si-rich
16_14	56.4 ± 2.0	19.3 ± 2.1	8.2 ± 0.8	13.5 ± 1.5	2.6 ± 0.3		0.77 ± 0.06	0.38 ± 0.05	1.1 ± 0.2	Pyroxene
22_09, core	57.0 ± 2.1		2.0 ± 0.2	9.0 ± 1.0	7.0 ± 0.8	24.0 ± 6.0	0.58 ± 0.11 ^b	—	—	Grossite
22_09, 2nd phase	53.0 ± 1.9	19.0 ± 2.1	6.0 ± 0.6	8.0 ± 0.9	10.0 ± 1.1	4.0 ± 1.0	0.74 ± 0.05 ^b	—	—	Mellilite
22_09, 3rd phase	60.0 ± 2.2	26.0 ± 2.9	3.0 ± 0.3	11.0 ± 1.2			0.67 ± 0.06	0.21 ± 0.02	0.5 ± 0.1	Si-rich
26_06	63 ± 2.3	21.2 ± 2.3	6.6 ± 0.6	6.6 ± 0.7	2.6 ± 0.3		0.59 ± 0.05	0.5 ± 0.06	0.6 ± 0.1	Si-rich
26_10a	56.7 ± 2.0	20.9 ± 2.3	10.8 ± 1.0	9.8 ± 1.1	1.7 ± 0.2		0.76 ± 0.06	0.52 ± 0.06	1.0 ± 0.1	Pyroxene
26_11	55.6 ± 2.0	18.6 ± 2.0	12.7 ± 1.2	10.9 ± 1.2	2.1 ± 0.2		0.80 ± 0.06	0.54 ± 0.06	1.3 ± 0.2	Intermediate
26_12	55.8 ± 2.0	18.3 ± 2.0	18.4 ± 1.7	6 ± 0.7	1.5 ± 0.2		0.79 ± 0.06	0.75 ± 0.09	1.3 ± 0.2	Intermediate
27_02	55.1 ± 2.0	11.3 ± 1.2	23.9 ± 2.2	7.7 ± 0.9	2.0 ± 0.2		0.81 ± 0.06	0.76 ± 0.09	2.8 ± 0.4	Si-poor
27_06 core	57.8 ± 2.1	12 ± 1.3	13.2 ± 1.2	15 ± 1.7	2.0 ± 0.2			0.47 ± 0.06	2.4 ± 0.4	Fe-rich
27_06 rim	56.2 ± 2.0	16.9 ± 1.9	20.2 ± 1.9	5.5 ± 0.6	1.3 ± 0.1		0.78 ± 0.06	0.79 ± 0.10	1.5 ± 0.2	Intermediate
27_07	58.5 ± 2.1	18.7 ± 2.1	6.1 ± 0.6	11.6 ± 1.3	1.8 ± 0.2	3.3 ± 0.8	0.71 ± 0.05	0.34 ± 0.04	0.9 ± 0.1	Pyroxene
27_09	50.7 ± 1.8	18.3 ± 2.0	9.3 ± 0.9	19.8 ± 2.2	1.9 ± 0.2		0.97 ± 0.07	0.32 ± 0.04	1.6 ± 0.2	Intermediate
30_12	62.3 ± 2.2	28.9 ± 3.2	4.3 ± 0.4	4.5 ± 0.5			0.61 ± 0.06	0.49 ± 0.06	0.3 ± 0.1	Si-rich
30_23	60 ± 2.2	30.4 ± 3.3	5.9 ± 0.6	2.9 ± 0.3	0.7 ± 0.1		0.67 ± 0.06	0.67 ± 0.08	0.3 ± 0.1	Si-rich
31_09a	60.1 ± 2.2	24.2 ± 2.7	8.7 ± 0.8	2.7 ± 0.3	4.3 ± 0.5		0.66 ± 0.05	0.76 ± 0.09	0.5 ± 0.1	Si-rich
31_09b	61.9 ± 2.2	21.6 ± 2.4	11.9 ± 1.1	3.8 ± 0.4	0.8 ± 0.1		0.62 ± 0.05	0.76 ± 0.09	0.7 ± 0.1	Si-rich
31_09c	61.1 ± 2.2	22.3 ± 2.5	5.9 ± 0.6	5.9 ± 0.7	1.6 ± 0.2	3.2 ± 0.8	0.64 ± 0.05	0.5 ± 0.06	0.5 ± 0.1	Si-rich
31_16	57.9 ± 2.1	11.9 ± 1.3	14.9 ± 1.4	5.7 ± 0.6	2.9 ± 0.3	6.7 ± 1.7	0.73 ± 0.05	0.72 ± 0.09	1.7 ± 0.2	Olivine
32_03, core	54.5 ± 2.0	12.5 ± 1.4	8.5 ± 0.8	9.7 ± 1.1	1.6 ± 0.2	13.3 ± 3.3	0.66 ± 0.06 ^b	—	—	Hibonite?
32_03, rim	56.4 ± 2.0	24.9 ± 2.7	6.3 ± 0.6	6.9 ± 0.8	2.4 ± 0.3	3.1 ± 0.8	0.77 ± 0.06	0.48 ± 0.06	0.5 ± 0.1	Si-rich
32_08	55.3 ± 2.0	8.9 ± 1.0	30.0 ± 2.8	2.7 ± 0.3		3.9 ± 1.0	0.82 ± 0.06	0.92 ± 0.12	3.7 ± 0.5	Si-poor
32_13	59.8 ± 2.2	18.2 ± 2.0	12.7 ± 1.2	3.5 ± 0.4		5.7 ± 1.4	0.67 ± 0.05	0.78 ± 0.10	0.9 ± 0.1	Pyroxene
33_13	56.5 ± 2.0	12.9 ± 1.4	15.5 ± 1.5	15.1 ± 1.7			0.77 ± 0.05	0.51 ± 0.06	2.4 ± 0.3	Si-poor
34_15	63 ± 2.3	13.9 ± 1.5	18.9 ± 1.8	4.2 ± 0.5			0.59 ± 0.04	0.82 ± 0.10	1.7 ± 0.2	Olivine
35_19	54.8 ± 2.0	21.0 ± 2.3	7.4 ± 0.7	15.9 ± 1.8	0.9 ± 0.1		0.82 ± 0.06	0.32 ± 0.04	1.1 ± 0.2	Pyroxene
31_13	52.6 ± 1.9	21.4 ± 2.4	16.8 ± 1.6	9.3 ± 1.0			0.90 ± 0.07	0.64 ± 0.08	1.2 ± 0.2	Pyroxene
33_19	58.6 ± 2.1	14.4 ± 1.6	17.4 ± 1.6	8.1 ± 0.9	1.4 ± 0.2		0.70 ± 0.05	0.68 ± 0.08	1.8 ± 0.2	Olivine
35_11	58.2 ± 2.1	25.5 ± 2.8	6.7 ± 0.6	8.2 ± 0.9	1.4 ± 0.2		0.72 ± 0.06	0.45 ± 0.05	0.6 ± 0.1	Si-rich
27_05	58.1 ± 2.1	6.2 ± 0.7	2.4 ± 0.2	4.8 ± 0.5	1.8 ± 0.2	25.7 ± 6.4	0.70 ± 0.11	—	—	Hibonite
28_01	57.1 ± 2.1	7.0 ± 0.8	3.3 ± 0.3	2.7 ± 0.3	2.8 ± 0.3	27.1 ± 6.7	0.75 ± 0.12	—	—	Hibonite
35_17	52.9 ± 1.9	7.3 ± 0.8	2.2 ± 0.2	5.7 ± 0.6	0.8 ± 0.1	32.2 ± 8.0	0.91 ± 0.16	—	—	Corundum

^a Ca contents should be regarded as intrinsic to the grains if associated with Al. Otherwise it likely represents a terrestrial contamination.^b The Fe abundance has not been included in this ratio.

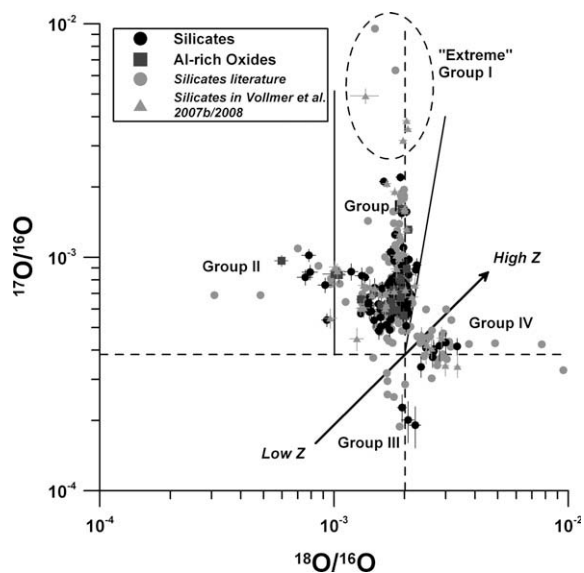


Fig. 1. Oxygen isotopic compositions of presolar silicate and oxide grains in Acfer 094. Data from this study are compared to presolar silicate data from the literature (NanoSIMS data only: Messenger et al., 2003; Mostefaoui and Hoppe, 2004; Floss et al., 2006; Nguyen et al., 2007b; Bland et al., 2007; Bose et al., 2008a,b; Yada et al., 2008; Floss and Stadermann, 2009). The SNII olivine from Messenger et al. (2005) is not plotted (off-scale). “Extreme” Group I grains are circled by a dotted ellipse. The approximate ranges of the O isotope groups defined by Nittler et al. (1997) and the evolution of the O isotopes from low to high metallicity Z based on GCE considerations are shown for comparison.

and b). They also contain Mg, Fe and Si in the % range, but those minor components are most probably not intrinsic to the grains of interest, but due to surrounding material. The three grains with quantitative Auger data are classified as two hibonites (CaAl_2O_9) and one corundum (Al_2O_3), in the qualitative data set there are two corundum-like grains, one hibonite-like and one spinel-like (MgAl_2O_4) grain.

About half of the Fe- and Mg-rich silicates and four out of seven measured presolar oxides contain variable amounts of Ca between 0.7 and 4.3 at.%, and a few grains have Al contents in the % range. Other Auger investigations of presolar silicates from other primitive meteorites detected fewer grains with Ca enrichments (Nguyen et al., 2008b; Floss and Stadermann, 2009). In addition, investigations of grain size separates from Acfer 094 also do not observe the presence of Ca in many presolar silicates (Bose et al., 2008a, 2009). In an effort to understand the source of this discrepancy, we examined randomly chosen grains from the matrix of our thin section and from a different thin section of the same meteorite. The Auger measurements show that 22 out of 30 measured grains from our section contained Ca, whereas only 3 out of 20 grains from the other section had Ca. These results indicate that our thin section is clearly contaminated with Ca compared to the other section. Terrestrial alteration can provide one possible explanation for the discrepancy. The presence of Ca in the grains analyzed here could be of secondary origin due to aqueous alteration, which leads to the precipitation

of carbonates. Acfer 094 has not experienced significant parent body alteration, as inferred from its low abundance of hydrated silicates (Newton et al., 1995), but may indeed be terrestrially altered (Alexander et al., 2007; Bland et al., 2008). If the piece of meteorite that was used for the production of our thin section originated from a location within the original stone closer to the surface and was, therefore, more heavily infiltrated by terrestrial water, this could account for the elevated Ca contents observed in the randomly selected grains and in the presolar grains from this section. We therefore conclude that observed Ca contents in presolar oxides and silicates in this study are most likely not of circumstellar, but of terrestrial origin, and marked all Ca contents in Table 3b as dubious. However, we cannot rule out the possibility that some Ca is primary. It is most likely that Ca is an intrinsic component of the grains in those cases in which the Ca is associated with Al (i.e., in the oxides, the two complex grains and in some other grains with relatively high Al contents).

3.4.2. Complex grains

Three grains consist of presolar refractory oxide grains attached to presolar silicates and are, thus, described as “complex” (Fig. 8). Grain 7_04 was the first grain of this kind to be discovered, but the Auger Nanoprobe was not available at that time (Vollmer et al., 2006). Unfortunately, this grain could not be relocated in the TEM, after it was extracted by the focused ion beam technique from the meteorite thin section, leaving its mineralogical constitution unclear. This could either mean that not much of the grain was left after the NanoSIMS measurement or that we did not cut the grain exactly in its center. FE-SE imaging (Fig. 8b) shows that the central grain, $\sim 500 \times 350 \text{ nm}^2$ in size, is triangular, on whose three sides silicate material has been accreted. In a subsequent NanoSIMS re-examination before preparation for TEM, the ionization efficiency of Ca was too low to obtain accurate statistics, but the central grain itself displayed low Mg count rates, pointing to corundum, grossite (CaAl_4O_7) or hibonite rather than spinel. The core grain is surrounded by small particles with bright contrast in the SEM (Fig. 8b). The O-isotopic composition in the surrounding silicates is more anomalous (i.e., higher $^{17}\text{O}/^{16}\text{O}$ and lower $^{18}\text{O}/^{16}\text{O}$ ratios) than in the core oxide (Fig. 8a). This may be an artifact due to dilution of the measured isotopic ratios in the core with the particles, which presumably have normal isotopic compositions.

A second complex grain, 22_09, consists of at least three different Ca–Al–Si-bearing subphases and was examined in detail by Auger electron spectroscopy (Figs. 8c and 9). Here, isotopic compositions of the different phases are the same throughout the entire grain. The phase on the left-hand side of the grain is triangular like the core in 7_04 and consists mostly of O, Al and Ca with minor contributions of Fe and Mg (see Table 3b) with a stoichiometry resembling grossite. The cation/O ratio of the grain is 0.58 ± 0.09 , which is within errors of the expected value for grossite (0.71), and the Ca/Al ratio is compatible with this identification as well ($\text{Ca}_{1.06}\text{Mg}_{0.3}\text{Al}_{3.64}\text{O}_7$). The Fe content of this grain could be due to surrounding or overlying phases that are not necessarily part of the isotopically

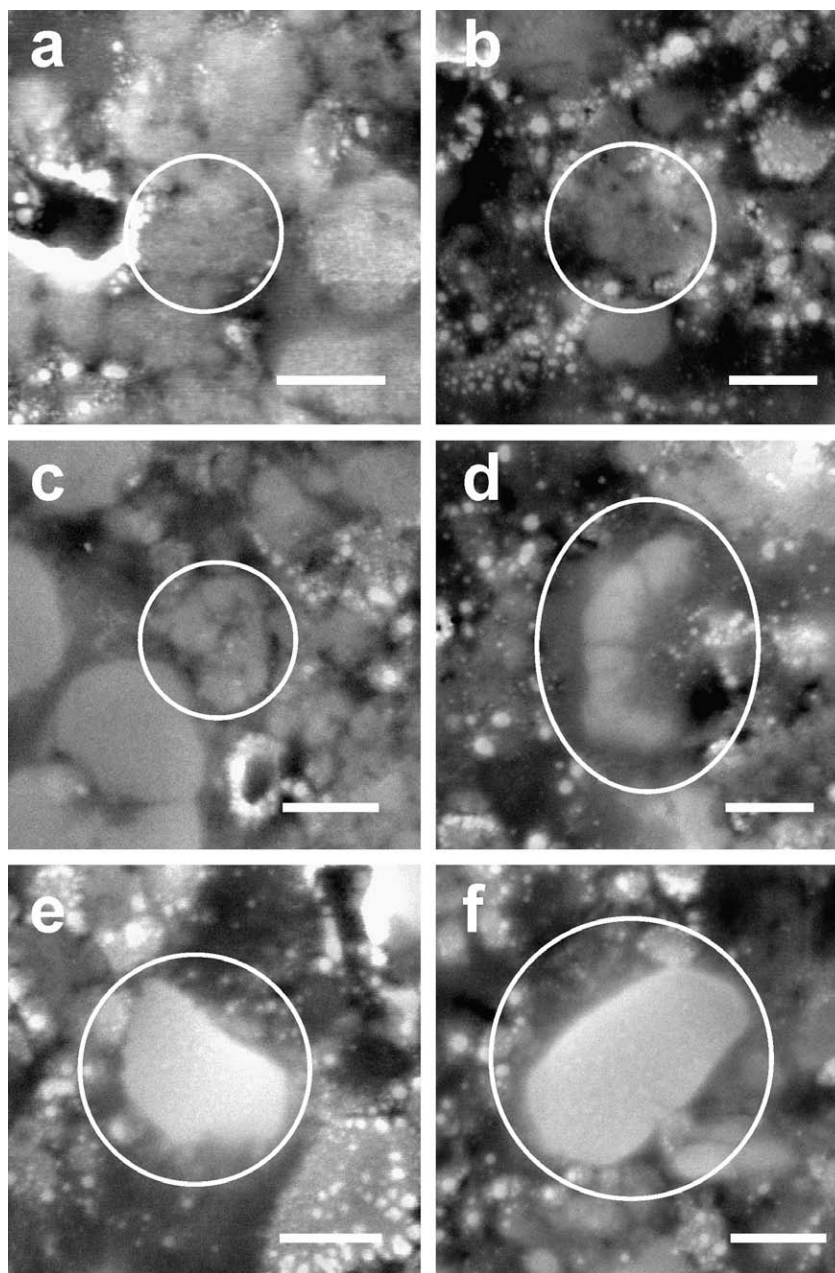


Fig. 2. FE-SE images of different morphologies of presolar silicate grains (circled) from this study. Polyaggregate/irregular grains: (a) grain 14_09, (b) grain 27_09, (c) grain 33_19; one smooth, elliptical grain with visible cracks: (d) grain 26_06; and two elliptical, smooth, platy grains: (e) grain 30_12 and (f) grain 30_23. Scale bar represents 200 nm in each image.

anomalous region and was therefore not included in this mineral formula calculation. The central phase of this complex grain is dominated by O, Si and Ca with minor contributions of Fe, Mg and Al and most resembles melilite ($\text{Ca}_2\text{Al}_2\text{SiO}_7$, gehlenite endmember— $\text{Ca}_2\text{MgSi}_2\text{O}_7$, åkermanite endmember). The cation/O ratio (again without the Fe content) matches this identification very well (0.74 ± 0.05 compared to the expected value of 0.71) and the stoichiometry is similar to melilite, although the Ca content is a bit too low and the Si content too high ($\text{Ca}_{1.28}\text{Al}_{0.5}\text{Mg}_{0.77}\text{Si}_{2.44}\text{O}_7$). The third part of grain 22_09 to the right consists

of a complex mixture of non-stoichiometric subphases, as is evident from the Ca-rich “hot spot” in one corner and the heterogeneous distribution of Si (Fig. 9). It should therefore be regarded as a non-stoichiometric silicate with a relatively high Si content not compatible with standard silicate minerals ($(\text{Mg} + \text{Fe})/\text{Si} = 0.5 \pm 0.1$). Because the minerals in this complex presolar assemblage are also found in Ca–Al-rich inclusions (“CAIs”) from meteorites, this complex grain can be described as the first, presolar CAI. Unfortunately, the grain was lost during preparation for further TEM observations.

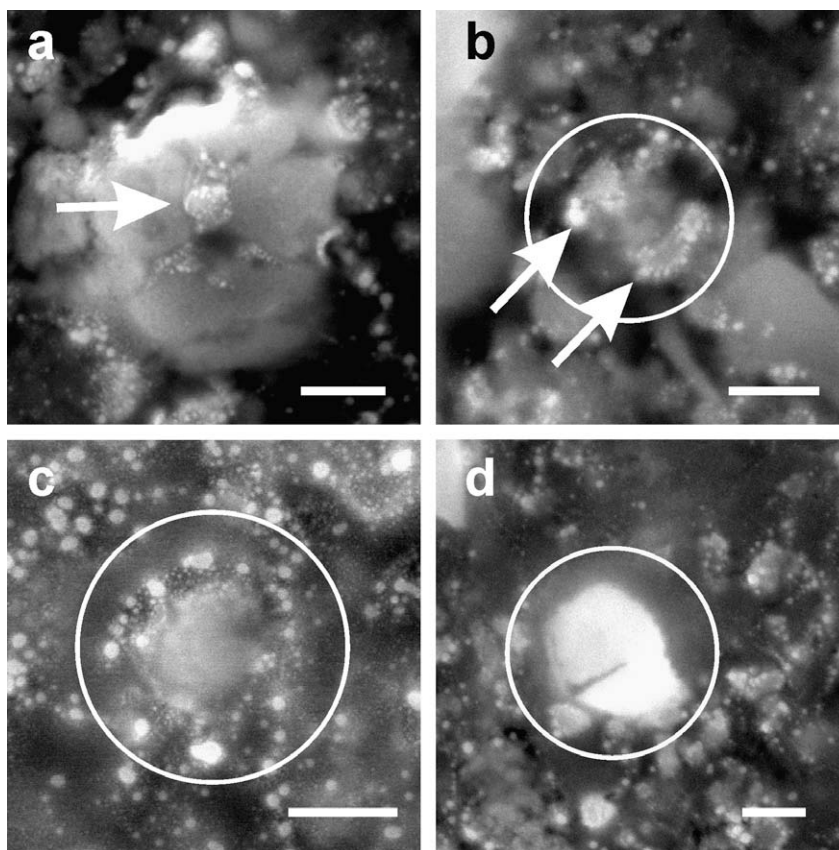


Fig. 3. FE-SE images of specific features of presolar silicates. (a) Elliptical grain 27_06 with Fe oxides or Fe metal (arrow-marked) in the center, (b) irregular grain 31_02 with an accreted rim (arrows), (c) isometric grain 13_15 surrounded by small nanoparticles, and (d) elliptical grain 31_09b disrupted by a crack. Scale bars represent 200 nm.

The third grain (32_03, Figs. 8d and 10) is characterized by a small area with a high Al content and an overall rather complex appearance as can be seen from the Auger elemental maps: the attached grain to the north of the Al-rich region appears to be a silicate with approximately equal abundances of Mg and Fe and again a relatively high Si content ($(\text{Mg} + \text{Fe})/\text{Si} = 0.5 \pm 0.1$), which is partly enclosed by another Al-rich phase in two long bars (Fig. 10). It is difficult to calculate the mineral formula for this central grain, because the high Si content indicates that the silicate phase contributes to this analysis. However, the Al/Ca ratio of 8.3 points to hibonite instead of grossite or corundum as the most probable identification.

4. DISCUSSION

4.1. Oxygen isotopic compositions of presolar silicate and oxide grains

The fraction of Group I grains in this work (81%) is similar to what has been found from other in situ studies of primitive meteorites (e.g., Mostefaoui and Hoppe, 2004; Nguyen et al., 2007b) and also what is observed for presolar oxide grain separates (Nittler et al., 1997, 2008). It has been argued (e.g., Nittler et al., 1997, 2008) that most presolar silicates and oxides derive from AGB stars of close-to-solar

or slightly lower-than-solar metallicity and about 1.1–2.5 M_{\odot} based on comparisons with model predictions for the first and second dredge-up in red giant stars (Boothroyd and Sackmann, 1999). However, Nittler et al. (2008) pointed out that red supergiants ($M > 8 M_{\odot}$) might also reproduce observed Group I oxygen isotopic ratios, and that these stars might contribute as much as 2/3 of the O-rich interstellar dust budget (Kemper et al., 2004). Based on O-isotopic compositions and inferred $^{26}\text{Al}/^{27}\text{Al}$ ratios from 10^{-4} to 10^{-2} about 15% of the presolar oxide population could indeed originate from red supergiants (Nittler et al., 2008). On the other hand, it has also been argued that dust from red supergiants may not survive the shock wave from the subsequent SNI explosion of the star (Zhukovska et al., 2008). Since not only O- and Al-, but also Si-isotopic compositions are expected to be similar in grains from low-mass AGB stars and red supergiants, actual data cannot be used to shed more light on the issue of distinguishing between a low- and high-mass red giant star origin. Recent work by Gail et al. (2009) indicates that intermediate-mass AGB stars (4–8 M_{\odot}) should contribute about half of the presolar oxide and silicate population, as they are as efficient in O-rich dust production as low-mass AGB stars. Based on stellar evolution models, such stars are expected to experience hot bottom burning, which would dramatically change their isotopic compositions, i.e., lower their

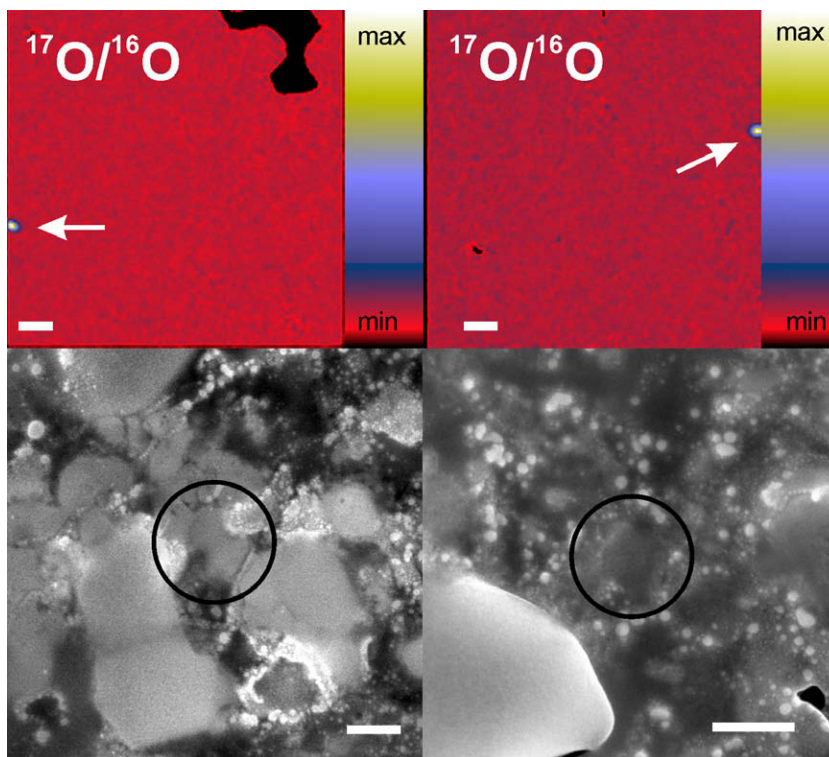


Fig. 4. Morphologies of “extreme” Group I grains. NanoSIMS $^{17}\text{O}/^{16}\text{O}$ ratio images (upper panels) and FE-SE images (lower panels) of the extreme Group I grains 13_13 (left panels) and 13_16 (right panels). Scale bar represents 1 μm in the NanoSIMS ratio images and 200 nm in the SE images.

$^{18}\text{O}/^{16}\text{O}$ to about 10^{-6} – 10^{-7} and enrich $^{17}\text{O}/^{16}\text{O}$ to at least 10^{-3} (Lugaro et al., 2007), which is not observed in the majority of presolar O-rich grains. To date, there is no satisfactory explanation for the apparent lack of such grains in

the presolar silicate/oxide population. It is possible that the stars that contributed grains to the solar nebula were not representative of the stars that deliver material to the ISM (Gail et al., 2009). Alternatively, these grains might

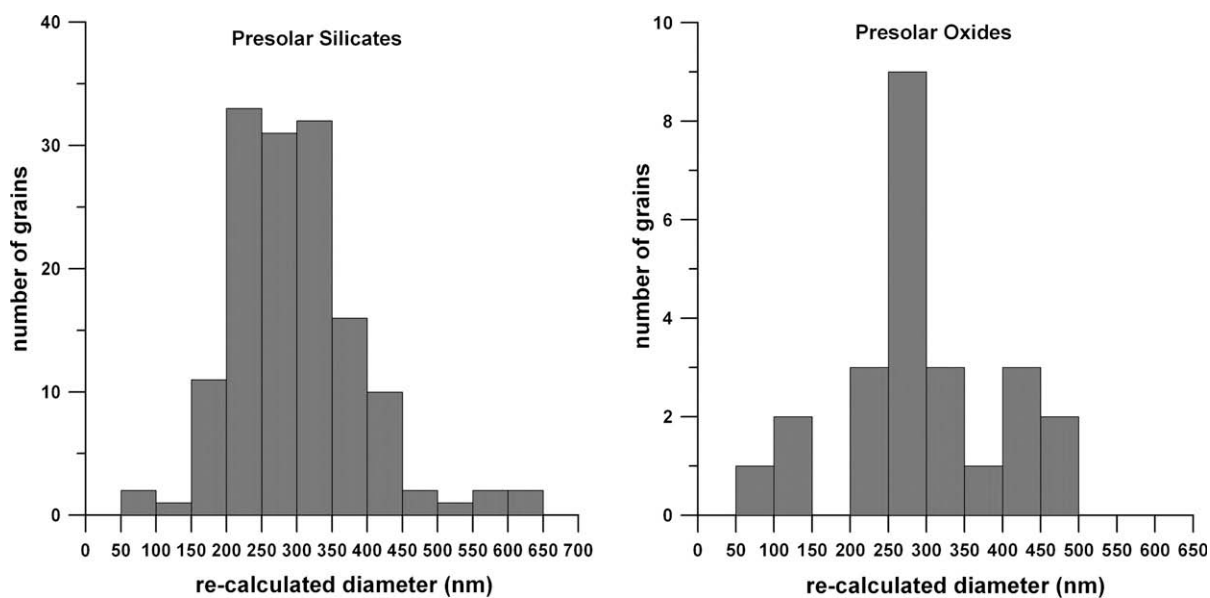


Fig. 5. Size distribution of presolar silicates and Al-rich oxides in Acfer 094. The cutoff to the lower diameters is due to the fact that the smallest grains ($< \sim 150$ nm) are not efficiently detected by the NanoSIMS. For irregular or elliptical grains, the re-calculated diameter refers to the diameter of a sphere with the same cross-sectional area.

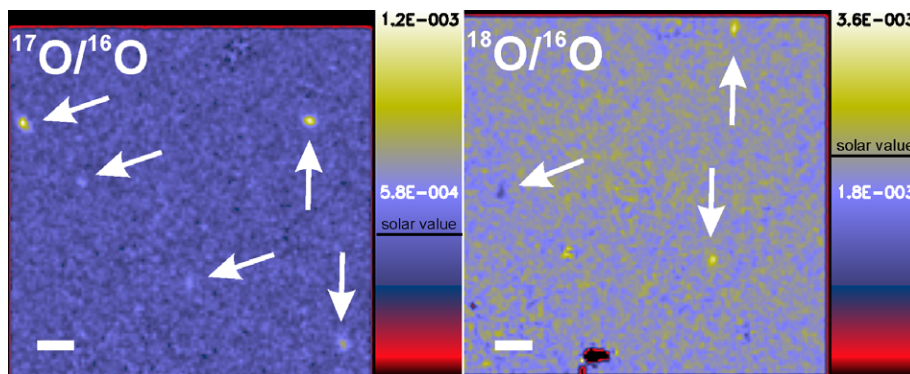


Fig. 6. NanoSIMS $^{17}\text{O}/^{16}\text{O}$ and $^{18}\text{O}/^{16}\text{O}$ ratio images of presolar silicates in the field 26_10 (left) and 22_10 (right), respectively. In most such clustering cases the clustered grains are from the same isotope group (as in 26_10), but in three cases the grains are from different groups (e.g., Groups I and IV in field 22_10). The red and black rim marks the edge of the analyzed area, some other anomalous spots are either artifacts due to morphology effects or do not fulfil the 4σ criterion. Scale bar represents 1 μm . (For interpretation of the references to color in this figure legend, the reader is referred to the web version of this article.)

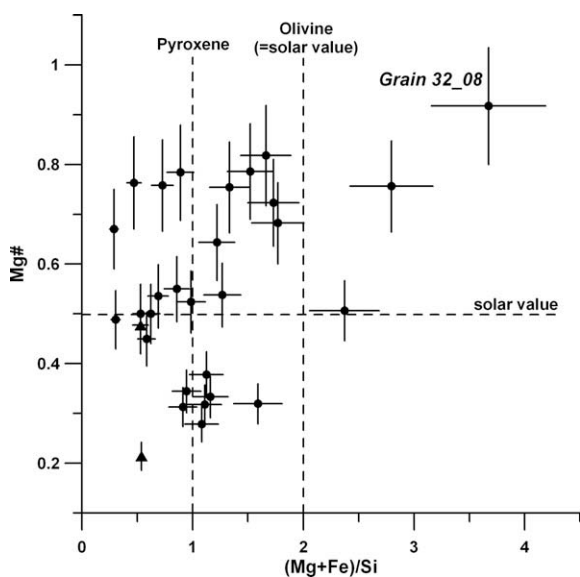


Fig. 7. Mg-Fe-Si element abundances of presolar silicates with quantified Auger spectra (1σ errors). Most of the grains have non-stoichiometric compositions over a large elemental range, but tend to scatter around pyroxene-like and intermediate compositions. The two triangular data points are from the silicate material of the complex grains.

be smaller than the stardust silicates from low-mass AGB stars, which could make their detection even by NanoSIMS challenging. Clearly, more modelling and additional isotopic measurements are needed to evaluate the apparent mismatch between predicted dust production rates of intermediate-mass AGB stars and observed grain data.

Three grains in our study have close-to-normal $^{18}\text{O}/^{16}\text{O}$ ratios, but $^{17}\text{O}/^{16}\text{O}$ ratios higher than 3×10^{-3} (“extreme” Group I, Vollmer et al., 2008), which lies in the upper range of model predictions for the first dredge-up in red giant stars. As has been discussed by Nittler et al. (2008) and Vollmer et al. (2008), the O- and Si-isotopic data of these extremely ^{17}O -rich grains might indicate an origin in binary

star systems, in which mass was transferred from a low-mass AGB star or from a nova explosion to a main sequence star. It is difficult to form such grains directly in nova ejecta, as predicted isotopic compositions are more extreme by at least one order of magnitude (José and Hernanz, 2007). An origin from higher mass ($\sim 3 M_{\odot}$) AGB stars is another possibility to explain the O- and Si-isotopic data of these grains (Vollmer et al., 2008). A fourth “extreme” Group I grain (“1_07”) from Acfer 094, for which no isotopic data other than for O are available, has an unusual, high-pressure structure (Vollmer et al., 2007b), but this grain has most probably been modified in a circumstellar or interstellar shock wave. From the current database it is not possible to evaluate in more detail the origins of these “extreme” Group I grains.

The abundance of Group II silicates (7%) is comparable to what has been found by Nguyen et al. (2007b). Low $^{18}\text{O}/^{16}\text{O}$ ratios are generally explained either by a low initial parent star metallicity or through destruction of ^{18}O by extra mixing processes such as cool bottom processing (Nollett et al., 2003). It is interesting to note that four out of 11 Group II grains (including one complex grain) are Al-rich oxides, which represents a higher fraction than Al-rich oxides among the total population of O-rich stardust (1/6 in this work). However, the statistical significance of this observation is low given our limited data set.

The Group III abundance (2%) in this study is a bit lower than what was found by Nguyen et al. (2007b), and none of the three silicates could be relocated for further characterization. The origins of Group III grains are still not well constrained, as nearly no isotopic data other than for O are available so far. The three Group III silicates in this study are characterized by $^{17}\text{O}/^{16}\text{O}$ ratios around 2×10^{-4} and close-to-solar $^{18}\text{O}/^{16}\text{O}$, which is similar to the results of Nguyen et al. (2007b) on Group III silicates. The most probable stellar sources are AGB stars of lower mass and metallicity than the parent stars of the other grains, because GCE models predict lower-than-solar $^{17,18}\text{O}/^{16}\text{O}$ ratios for these stars. However, Nittler (2007) and Nittler et al. (2008) recently proposed a SNII as a possible alternative for the ori-

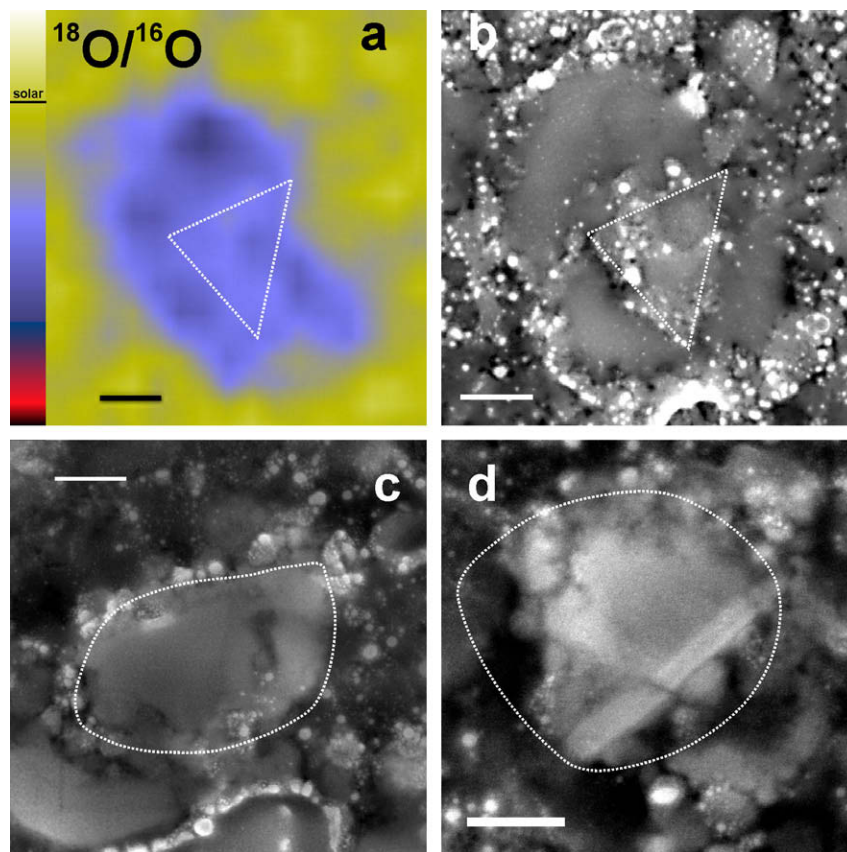


Fig. 8. NanoSIMS ratio image of grain 7_04 and FE-SE images of the three complex grains. (a) The $^{18}\text{O}/^{16}\text{O}$ ratio image of grain 7_04 indicates different isotopic compositions in rim and center, (b) FE-SE image of about the same area as (a) (grain 7_04) with a triangular core (marked by the dotted line) decorated by bright particles, (c) FE-SE image of grain 22_09 with the outline of the O isotope anomaly, (d) FE-SE image of grain 32_03 with the outline of the O isotope anomaly. All scale bars represent 200 nm.

gin of some Group III grains, especially for those with $^{17}\text{O}/^{18}\text{O}$ ratios below the predicted GCE line, which applies to the grains from this study. In this model, a large fraction of Group IV grains (see below) and some Group III grains could, in fact, be explained by mixing of distinct zones (i.e., a ^{16}O -rich endmember and material from the H-rich envelope) in a single SNeII. One Group III grain, whose Si isotopic composition was measured by Nguyen et al. (2007b), is characterized by large enrichments in both ^{29}Si and ^{30}Si , which probably rules out a low-metallicity source, at least for this grain. Additional isotopic measurements are necessary to test these assumptions on the origins of Group III grains.

The Group IV silicates (10%) from this study are moderately enriched in ^{18}O and the O isotope data overlap with literature data of Group IV silicates (Fig. 1). The abundance of Group IV grains is less by more than 2σ than what has been found by Nguyen et al. (2007b). This is also in contrast to IDPs and Antarctic micrometeorites, where a higher fraction (33–37%) of presolar silicates derive from this O isotope group (Messenger et al., 2003, 2005; Floss et al., 2006; Yada et al., 2008). All Group IV grains in this study are silicates, which is surprising as Group IV oxides have indeed been found with a similar abundance (e.g., Nit-

ler et al., 1997, 2008). But, given that our data set consists of only 20 Al-rich oxide grains, this observation has limited statistical significance. Group IV grains have drawn considerable attention in recent years (Nittler, 2007; Bose et al., 2008b; Vollmer et al., 2008), because their origins are poorly constrained from O isotope data alone. Multi-element (O, Mg, Ca, K) isotope measurements on the same grains have provided clear evidence of a SNeII origin for some Group IV oxides (Nittler et al., 2008), as originally proposed by Choi et al. (1998). Further support comes from the ^{28}Si enrichments in most of our Group IV silicates, which point to a close relationship with SiC and graphite grains from SNeII (Vollmer et al., 2008).

From the fact that some Group IV (and Group III, see above) silicates and oxides appear to lie on a single mixing line, connecting a ^{16}O -enriched and a $^{17,18}\text{O}$ -enriched reservoir, Nittler (2007) speculated that these grains might have originated from a single SNeII. This could also explain the heterogeneous distribution of Group IV grains in various primitive solar system samples, i.e., in meteorites compared to IDPs, if these grains were injected into the solar nebula in a single event and were not well-mixed (Yada et al., 2008). However, an extensive study on the distribution of Group IV silicates in various primitive solar system materi-

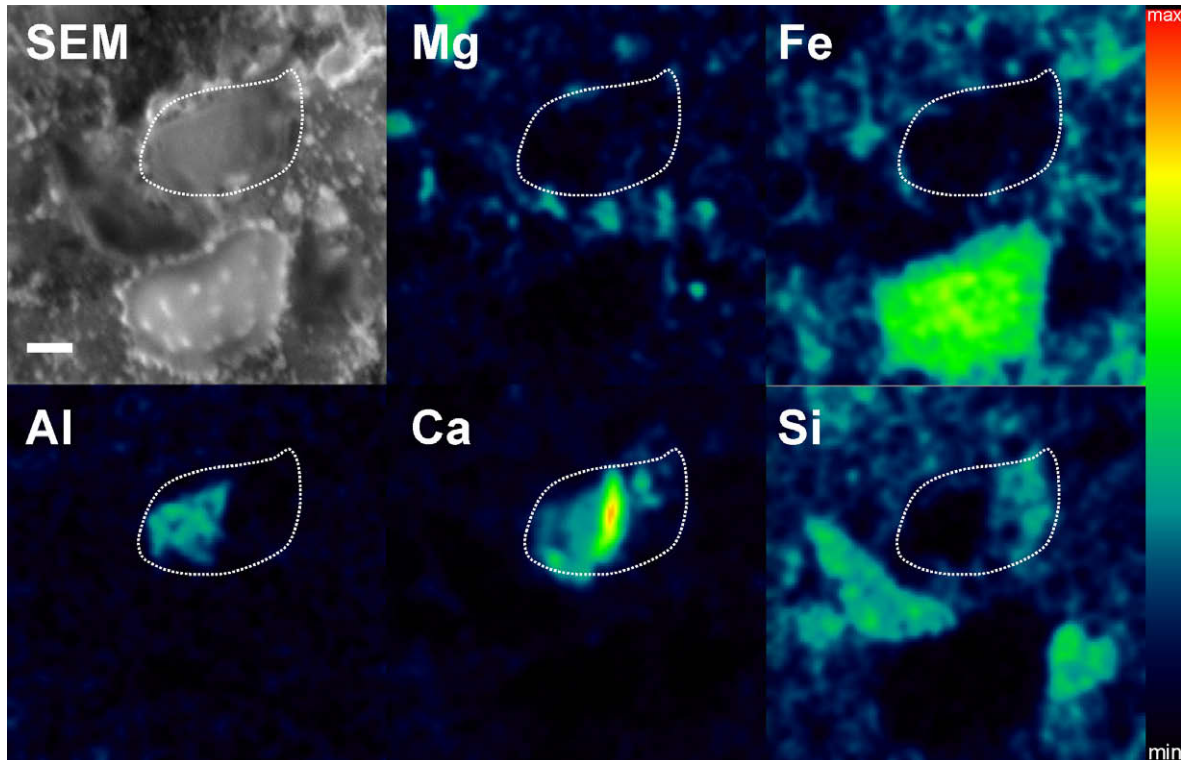


Fig. 9. FE-SE image of the presolar CAI 22_09 and corresponding Auger electron elemental maps. The outline of the O isotope anomaly is marked in all elemental maps. Fe and Mg appear to be absent in the grain, but this is due to the automatic scaling of the color scheme, indicated by the bar on the right side, which displays the range from lowest to highest abundance for each element in the whole image. Al, Ca and Si are heterogeneously distributed. Scale bar represents 200 nm and refers to all images. (For interpretation of the references to color in this figure legend, the reader is referred to the web version of this article.)

als, which could further support such a SNII scenario, is still lacking because of limited data. Additional support for the proposed SNII origin comes from the distinctive morphologies of Group IV grains (see Section 4.2).

4.2. Shapes of silicate stardust grains

Laboratory studies of synthetic analogues have shown that silicate condensates often consist of small (20–50 nm), spherical particles bound to fluffy fractal-like structures (Colangeli et al., 2003). In contrast, single crystals of forsterite may condense along the crystallographic *c*-axis resulting in elongated dust grains, which could explain the elliptical shapes of this type of dust grain (Fabian et al., 2001; Takigawa et al., 2008). Other grain types may condense preferentially along one crystallographic axis in an analogous way. Therefore, elliptical or spherical grain shapes in this study might indicate similar condensation pathways leading to single phases that are not composed of smaller sub-particles. We do not know the crystallinities of the grains in most cases, and a spherical shape does not necessarily indicate formation by condensation. But if we assume that the shapes of our elliptical grains have not been strongly altered since their circumstellar formation, their shapes could indicate a primary condensation feature in agreement with the laboratory experiments for single crystals mentioned above. Our FE-SE images also suggest that these dust grains are more stable than the surrounding ma-

trix. In our data set Mg-rich grains ($Mg\# > 0.5$) are more likely to have elliptical, smooth shapes than more Fe-rich grains (14 out of 18 Mg-rich grains in the quantified Auger data set). Mg-rich grains are predicted to form under equilibrium conditions (e.g., Gail, 2003) at high temperatures likely leading to the precipitation of crystalline grains. The combined high Mg contents and smooth, elliptical grain shapes suggests that these grains have experienced little secondary alteration and are direct condensates from the circumstellar atmosphere.

The majority of grains in this study, however, display highly irregular, polyaggregate-like morphologies. Such morphologies have also been observed in condensation experiments, where irregular aggregates are formed rather than single crystals (Rietmeijer et al., 2002; Colangeli et al., 2003). Irregular aggregate particle shapes, however, could also be the result of severe fragmentation during ISM passage, which has been proposed to be a dominant modification process of interstellar grains (Jones et al., 1996). Finally, such grains might also have been altered by secondary processes in the solar nebula or on the meteorite parent body (see Section 4.4.1). It is, therefore, not clear to what extent irregular, polyaggregate-like morphologies are primary condensation features similar to the fluffy aggregates from laboratory experiments, or are the result of secondary alteration in the ISM or the solar nebula. It is possible that all of these processes played a role in the formation of irregular grains.

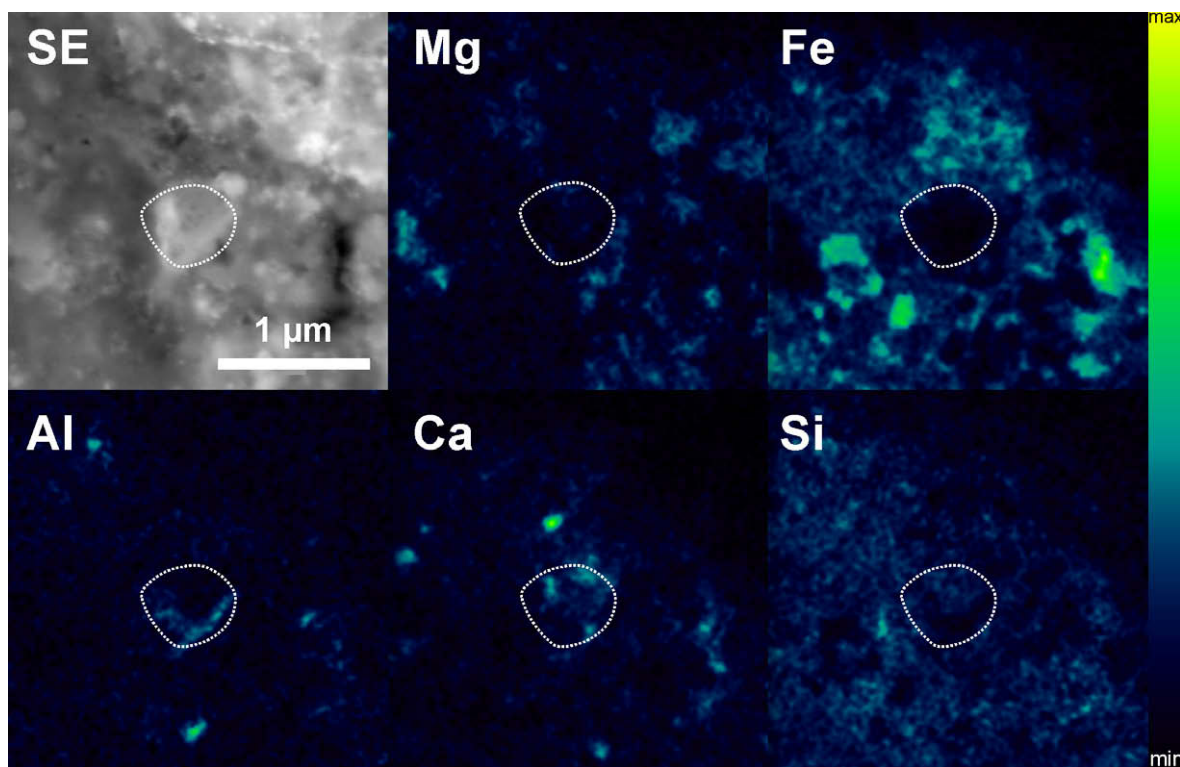


Fig. 10. FE-SE image of grain 32_03 and the corresponding Auger elemental maps. The complex nature of this grain (outlined by its O isotope anomaly in each frame) is obvious from the elemental maps, although count rates are lower than in Fig. 9 due to a shorter analysis time. Scale bar in the SE image refers to all frames.

There is no clear correlation between the isotopic compositions and morphologies of Group I/II grains. Group IV grains from this study, however, are generally smaller than 300 nm in at least one dimension and display predominantly irregular, polyaggregate-like shapes (14 out of 16 grains), which can be linked to their proposed SNeII origins (Messenger et al., 2005; Vollmer et al., 2008). The short condensation timescales in the rapidly expanding shells of SN explosions could hinder the formation of larger condensates. Because the Group IV grains are generally smaller, they may also be more easily overlooked, which could explain the differing abundances reported by various workers in different samples. They might then also be more susceptible to parent body alteration, which could also change their abundances in samples which experienced different degrees of alteration.

The Group III grains in this study, the rarest population of presolar grains, are even smaller, such that they could not be located in the SEM. This is consistent with the suggestion that these grains might come from SNeII for similar reasons as discussed above for Group IV grains (Nittler, 2007).

Finally, the highly ^{17}O -enriched “extreme” Group I grains are also smaller than 250 nm in at least one dimension, highly irregular in shape and harder to locate by FE-SE imaging within the matrix compared to less anomalous grains (Fig. 4). These grains might originate in binary star systems (Nittler et al., 2008; Vollmer et al., 2008), but it is not clear why grains that form around AGB stars in binary systems should be smaller than grains from single stars.

To date, there is only one TEM study of a grain of this type (Vollmer et al., 2007b), which revealed a highly unusual crystal structure not compatible with standard condensation models, indicating non-equilibrium formation conditions in a circumstellar or interstellar shock wave. This grain is therefore not suitable to test the binary star scenario, unless it was transformed in the shock wave emerging from the nova explosion that provided the ^{17}O atoms. If the grains, however, originated from higher mass ($\sim 3 M_{\odot}$) AGB stars, which might be consistent with measured O- and Si-isotopic ratios as well, their small sizes could explain the apparent lack of grains from these types of AGB stars. If AGB stars of higher masses tend to produce generally smaller grains than their lower mass counterparts, their identification within solar system samples could be more challenging, and these grains would then be under-represented in the presolar silicate data set. However, it is not clear why condensation around higher mass AGB stars should lead to smaller grain dimensions in general. Clearly, more comparative work on the morphological characteristics of different kinds of presolar dust grains and theoretical condensation models are needed to follow up on these observations.

4.3. Abundances and distributions of silicate and oxide stardust

Our matrix-normalized abundance of 163 ± 14 ppm for Acfer 094 is higher than the one reported by Nguyen et al.

(2007b) for the same meteorite (90 ± 35 ppm, uncorrected), whereas our presolar oxide abundance is lower (26 ± 6 ppm, compared to 55 ± 20 ppm in Nguyen et al., 2007b), although the values are compatible within 2σ errors. The discrepancy may be explained by the fact that presolar grain compositions were mostly determined from NanoSIMS $^{24}\text{Mg}^{16}\text{O}^-/^{16}\text{O}^-$ ratios in the grains in Nguyen et al. (2007b), whereas the classification in this work was mostly done by $^{27}\text{Al}^{16}\text{O}^-/^{16}\text{O}^-$ ratios in the NanoSIMS and by Auger electron spectroscopy. It is therefore possible that some grains in the work of Nguyen et al. (2007b) classified as oxides might actually be silicate grains, which would increase the silicate and decrease the oxide abundance in that study. Similarly, some Al-rich oxides identified only by NanoSIMS in our work may in fact be silicates. For the purpose of this discussion we assume that presolar silicate and oxide abundance determinations by Nguyen et al. (2007b) and in this work are the same within errors, and that silicates are ~ 6 times more abundant than oxides.

Further discussion on presolar silicate and oxide grain abundances was initiated by analysis of the CR3 chondrites QUE 99177 and MET 00426, which experienced virtually no aqueous or thermal alteration (Floss and Stadermann, 2009). Silicate/oxide ratios in these meteorites appear to be about 3–5 times higher than in Acfer 094 (20–33). A recent re-examination of the presolar silicate and oxide abundance in QUE 99177 (Nguyen et al., 2008a) revealed a lower silicate to oxide ratio (130–40 ppm, i.e., similar to the value described here), suggesting the possibility that the higher silicate to oxide ratios observed by Floss and Stadermann (2009) for QUE 99177 and MET 00426 compared to Acfer 094 are not representative of these meteorites as a whole. These differences could be due to different degrees of secondary alteration. A study of the presolar grain inventory of the CR chondrite NWA 852 indicated a lower silicate/oxide ratio than found in Acfer 094, most probably due to the high degree of aqueous alteration experienced by this meteorite (Leitner et al., 2009). Additional studies are needed to assess the initial silicate/oxide ratio in the solar nebula. It would also be interesting to compare this ratio with values in circumstellar environments, but identification of Al-rich phases by IR spectroscopy is problematic (Posch et al., 2007), because the bands are typically masked by strong silicate features, except in stars of unusual chemistry with strong silicate depletions (Maldoni et al., 2008).

Acfer 094 has evidently suffered from terrestrial alteration (Bland et al., 2008), whose influence on presolar grain abundances cannot be known. Nevertheless, this chondrite still contains among the highest amounts of presolar silicates reported so far, together with the CR3 chondrites MET 00426 (160 ppm) and QUE 99177 (130–220 ppm) (Nguyen et al., 2008a; Floss and Stadermann, 2009). Lower reported abundances for ordinary chondrites (10–20 ppm) (Mostefaoui et al., 2004; Tonotani et al., 2006), CI and CO chondrites (2 ppm and 36 ppm) (Marhas et al., 2006) and enstatite chondrites (20 ppm) (Ebata et al., 2007) most likely result from either insufficient spatial resolution of the applied analysis technique (i.e., IMS1270 with SCAPS

detector instead of NanoSIMS) or higher degrees of thermal metamorphism and/or aqueous alteration, as silicates are easily destroyed by these secondary processes. Destruction processes may have occurred either on the meteorite parent body or as the result of pre-accretionary processing in the solar nebula. The search for presolar material in a selection of Antarctic micrometeorites (Yada et al., 2008) yielded a presolar silicate abundance of ~ 50 ppm, which is also significantly lower than the Acfer 094 value. Generally, Antarctic micrometeorites predominantly show mineralogical and chemical affinities to carbonaceous chondrites rather than to IDPs, although some Antarctic micrometeorites with high presolar silicate abundances and ^{15}N -enrichments do appear to be similar to certain primitive IDPs (Floss et al., 2009).

The highest presolar silicate abundances that have been reported so far in any type of extraterrestrial matter are for a sub-group of IDPs with ^{15}N -enrichments (375 ppm) (Floss et al., 2006) and for a special set of IDPs collected during Earth's passage through the dust stream of comet Grigg-Skjellerup (Nguyen et al., 2007a). These "isotopically primitive" IDPs are characterized by components similar to those seen in the matrix of unaltered CR chondrites, although a clear connection between this IDP population and the CR chondrite group is still speculative. Given the relatively limited amount of material measured in IDPs to date (Floss et al., 2006), the presolar grain abundances of the meteorites described here, i.e., Acfer 094 and the CR3 chondrites, may be similar, within errors, to those of primitive anhydrous IDPs. Additional presolar grain searches in a variety of primitive extraterrestrial materials are necessary to confirm that presolar silicate and oxide abundances of ~ 150 – 200 ppm reflect the bulk abundance in the solar nebula.

To explore the statistical significance of the observed spatial clustering of presolar silicates in different matrix areas in our study, we calculated the probabilities resulting from a binomial distribution of finding two or more grains in the same analyzed field. We divide the $10 \times 10 \mu\text{m}^2$ sized field into squares of $300 \times 300 \text{ nm}^2$ size (resulting in $(10/0.3)^2$ squares), which is similar to the typical diameter of presolar silicate and oxide grains, and assume a probability of 0.000181 of encountering a presolar silicate (141 grains with an average area of $0.09 \mu\text{m}^2$ in a total search area of $70,500 \mu\text{m}^2$). This assumes that the detection efficiency in all analyzed fields is the same, which is not strictly correct, as the detection efficiency is influenced by the beam diameter and the instrumental settings of the NanoSIMS. Therefore, the probability of encountering a presolar silicate may vary from session to session. However, it is difficult to quantify such effects and for the purpose of this theoretical exercise, we assume that it is the same for all fields. The probability of finding two presolar silicates in one field is then 1.6%, i.e., in ~ 11 of all 705 analyzed fields. We have found 14 of these fields with two grains, which is in reasonably good agreement with statistical expectations. We should encounter 0.8 fields with three grains, which compares well with two such fields in our study. The detection of one field with five grains (Fig. 6), however, is statistically unexpected, as this should happen with a probability of

only 0.0002% in the 705 searched fields. This clustering is, thus, of high statistical significance. The calculated matrix-normalized abundance of stardust in this highly enriched area of $100 \mu\text{m}^2$ size is 0.35%, comparable to the highest reported abundance values in IDPs (Nguyen et al., 2007a).

Clustering of presolar grains has also been observed in CR chondrites (Floss and Stadermann, 2009) and IDPs (Floss et al., 2006, 2007; Nguyen et al., 2007a). Moreover, a recent investigation of presolar silicates in Antarctic micrometeorites revealed that most of the grains from one of the micrometeorites (9 silicates and 2 likely SiC) were found in a single $20 \times 20 \mu\text{m}^2$ area (Yada et al., 2008). It has been proposed that Group IV grains with a likely SNII origin might have been injected into the solar nebula in a single event (Nittler, 2007; Yada et al., 2008), which would explain their predominance in certain primitive materials (Yada et al., 2008). However, this does not explain the fact that we see grains from diverse origins (Group I and Group IV) within a single square of only $10 \times 10 \mu\text{m}^2$ size. The most straightforward explanation to this clustering is that the distribution of presolar materials (not only the Group IV population) in the solar nebula was heterogeneous on a very fine scale. Meteorites and IDPs that exhibit this heterogeneity then sampled different nebular reservoirs that were more or less enriched in presolar material in the evolving solar system. This heterogeneity could have been inherited from the distribution of grains in the parental molecular cloud, which implies that the surrounding matrix material is similarly of molecular cloud origin. The origin of the matrix material in primitive meteorites is still not well-understood. Alexander (2005) suggested that this matrix might represent a common presolar reservoir that has experienced minor to moderate alteration in the solar nebula. The observed clustering effects could support this scenario. Alternatively, these effects might be the result of differential secondary processing in separated regions of the meteorite parent body (Floss and Stadermann, 2009). Further comparative work on different solar system materials is necessary to follow up on this important observation.

4.4. Elemental composition of silicate and oxide stardust

4.4.1. Single grains

In this section we will discuss the elemental makeup of the presolar silicate and oxide grains studied by Auger electron spectroscopy. The three unusual, complex grains are examined in further detail in Section 4.4.2. The $(\text{Mg} + \text{Fe})/\text{Si}$ ratios of the measured grains can be used to test their affinity to pyroxene $(\text{Mg} + \text{Fe})/\text{Si} \sim 1$ or olivine $(\text{Mg} + \text{Fe})/\text{Si} \sim 2$. We did not include Ca in these ratios due to the contamination possibility discussed in Section 3.4.1, although this element also replaces Mg and Fe in silicate structures and would therefore shift calculated values. Grain stoichiometries can also be evaluated by the cation/O ratio, which should be 0.67 for pyroxene and 0.75 for olivine. Many of our grains have cation/O ratios that are higher than expected for either pyroxene or olivine, which may be an indication that some Fe is not an intrinsic part of the anomalous grain (see below).

Astronomical observations suggest that amorphous silicates are dominated by olivine-like compositions, whereas pyroxene is 3 times more abundant than olivine in the crystalline silicate fraction (Molster and Kemper, 2005). However, these relative abundances heavily depend on the optical reference parameters used and therefore bear respective uncertainties (Molster et al., 2002c). Our grain data predominantly scatter around pyroxene-like and intermediate values, with only two grains that are compatible with olivine-like compositions within errors. Recent TEM investigations of stardust silicates indicates that pyroxene-like grains are more likely amorphous and relatively abundant, whereas olivine-like grains are rarer and more likely crystalline (Stroud et al., 2008; Vollmer et al., 2009), which supports our observations. The results of our study are also consistent with the data by Floss and Stadermann (2009) that also indicated a higher abundance of pyroxene-like grains compared to olivine-like ones, although the grains in this study in general have lower Mg contents and a smaller total number of olivine-like grains.

There are several major formation possibilities for the pyroxene-like grains in these studies. Grains of originally olivine-like composition may have been converted to pyroxene-like grains during irradiation sputtering in the ISM combined with a preferential loss of Mg (Bradley, 1994; Demmyk et al., 2001). Alternatively, it is possible that these dust grains formed under non-equilibrium conditions and low temperatures in the circumstellar outflows, which is supported by TEM investigations on silicate stardust (Stroud et al., 2008; Vollmer et al., 2009), because the dust grains are heterogeneous on a very fine scale ($<50 \text{ nm}$), whereas ISM sputtering more likely leads to chemical homogenization (Keller et al., 2005; Vollmer et al., 2009). Finally, the grains could have been altered in the solar nebula, on the meteorite parent body, or during terrestrial weathering on Earth, which may also be consistent with their relatively high Fe contents (see below). The large scatter in $(\text{Mg} + \text{Fe})/\text{Si}$ ratios and Mg# (Fig. 7), in contrast to the data of Floss and Stadermann (2009), suggests that one or more of these processes has affected the grain population of Acfer 094. It is not possible yet to clearly elucidate the different processes that led to the predominance of pyroxene-like grains in the silicate stardust population, because we do not know the crystallinities of the grains in this study. The TEM analyses of a small subset of grains mentioned above, however, imply non-equilibrium condensation as the most probable cause.

The presence of grains with intermediate compositions in this study and other investigations (Floss and Stadermann, 2009) might be compatible with recent suggestions that interstellar silicates are expected to have a stoichiometry between that of olivine and pyroxene ($\text{O}/\text{Si} = 3.5$) (Min et al., 2007). However, the significance of this interpretation is limited by the fact that our grains are clearly more Fe-rich than expected in that work. To summarize these observations, it is evident from this study and other work that presolar silicates predominantly show pyroxene-like and intermediate chemistries, consistent with expectations for both circumstellar condensation models and secondary modification processes.

The origin of high Fe contents in presolar silicates is a major question and has also been discussed by other investigators (Bose et al., 2008a; Floss and Stadermann, 2009). It could be a primary condensation feature, i.e., the Fe could have condensed together with the silicates in circumstellar environments. Fe metal grains cannot be detected directly in the ejecta of evolved stars due to missing active vibrational modes (Molster and Kemper, 2005), although they are predicted to exist according to condensation calculations (Gail and Sedlmayr, 1999) and due to a high opacity of the dust shells in the near IR (Kemper et al., 2002). To explain the IR spectra, Fe could be present either as cations in the crystal lattice, as isolated dust grains or as particles surrounded by a glassy matrix (“astronomical/dirty silicates”). Those Fe-rich silicates usually form under non-equilibrium conditions at lower temperatures, which is a valid assumption for the fast cooling ejecta of dying red giant stars. If the measured Fe contents in the grains from this study are a primary condensation feature, this observation is indeed compatible with IR observations of circumstellar shells and theoretical predictions.

Secondary processing in the ISM, the solar nebula or on the meteorite parent body through thermal metamorphic reactions could also account for Fe in presolar silicates (Nguyen and Zinner, 2004). Re-condensation of Fe metal grains and silicate-metal equilibration during chondrule-forming processes accompanied by sulfurization and oxidation have been discussed as possible formation processes of Fe-rich material (e.g., Scott and Krot, 2003). The fact that many components within the Acfer 094 matrix are similarly surrounded by Fe-rich grains may support such a solar nebula origin. Aqueous alteration may furthermore result in the formation of magnetite framboids and sulfides adjacent to silicate grains (e.g., Boctor et al., 2003). Large, infiltrated presolar silicates like grain 27_06 indeed suggest that at least some Fe-rich material is of secondary nature. Similarly, as noted earlier, the higher-than-expected cation/O ratios may indicate the presence of secondary Fe in some of these grains. Fe-poor grains with fissures and cracks (Figs. 2 and 3) might then represent an intermediate position between two extremes: grains with no cracks, which are probably not strongly altered, and grains with filled cracks. However, Fe isotopic analyses of a presolar silicate and of an unusual presolar FeO grain yielded anomalous compositions (Mostefaoui and Hoppe, 2004; Floss et al., 2008) indicating that some Fe-rich presolar grains formed as primary condensates. The origin of the high Fe contents in the presolar silicates from this study remains ambiguous as additional Fe isotopic measurements have not yet been carried out.

The Auger quantification of the unusual grain 32_08 yielded a Mg/Si ratio of 3.4 (and a very low Fe content of 2.7 at.%). Two grains with similar high Mg/Si ratios have also been found in two CR3 chondrites (Floss and Stadermann, 2009). Such unusual Mg-rich grains suggest formation conditions under non-solar gas compositions and strong non-equilibrium conditions, possibly as metastable mixtures of Mg-rich oxides and silicates (Floss and Stadermann, 2009). This emphasizes that the conditions for grain formation in circumstellar environments are sometimes far from equilibrium.

Ten grains are depleted in both Mg and Fe compared to Si with $(\text{Mg} + \text{Fe})/\text{Si} < 0.7$, and are thus chemically similar to highly Si-enriched grains like 4_11 found by TEM (Vollmer et al., 2009). Other investigators have found grains of this type as well (Floss and Stadermann, 2009). These grains likely formed from a gas which was successively enriched in Si–O. If condensation of forsterite is followed by accretion of Fe metal grains, this would hinder the further reaction to form enstatite and enrich the gas in Si–O (Nagahara and Ozawa, 2008). Highly Si-enriched grains would then form as the result of strong non-equilibrium condensation conditions like the Mg-rich grains discussed above. Similar Si-rich and pure SiO₂ grains are also found in solar system chondrites, where they have been shown to form by such a fractional condensation mechanism (Hezel et al., 2006). Condensation calculations indicate that under low Mg/Si abundance ratios in the gas, quartz becomes a stable phase (Ferrarotti and Gail, 2001), which has not yet been detected as a presolar phase. Possible presolar SiO₂ grains have been recently identified by Auger electron spectroscopy, but no structural data are available yet (Bose et al., 2009; Floss and Stadermann, 2009). Silica might also be attributed to the 20.5 μm feature in IR spectra (Molster et al., 2002a) and has been found recently around protoplanetary disks, where it may have formed through incongruent melting of pyroxene (Sargent et al., 2009). It may therefore be only a matter of time until the first presolar quartz grain is identified and confirmed by TEM.

We can compare these presolar silicates with high Si contents with GEMS grains found in IDPs, which might represent the best match to “astronomical/dirty” silicates described above, but whose origins are still poorly constrained (Bradley, 1994; Bradley et al., 1999). The majority of GEMS grains have solar isotopic compositions, while only a few have a proven circumstellar origin as indicated by isotopic anomalies (Messenger et al., 2003). On the other hand, a solar isotopic composition does not necessarily exclude an interstellar origin (Bradley and Dai, 2004; Keller and Messenger, 2008). GEMS grains usually have sulfur contents above the 2–3 at.% level, but there is also a continuous distribution to grains with very low sulfur contents, which are generally rarer (Keller et al., 2005). The shapes of some grains in this study are similar to GEMS with regard to their polyaggregate- or fractal-like geometries. However, sulfur is below the detection limit in all grains but one. These grains may represent an unusual sulfur-poor sub-population of GEMS grains, similar to those reported by Vollmer et al. (2009) based on TEM observations. However, whereas high-sulfur GEMS grains from IDPs are well-documented, no GEMS with high-sulfur contents (>1 at.%) from primitive meteorites have yet been unambiguously identified by TEM (Vollmer et al., 2009), and further studies are clearly necessary to understand the reason for this discrepancy.

4.4.2. Complex grains

It is known from condensation theory that it is thermodynamically difficult to condense silicates directly from the gas phase, thus imposing the need for seed nuclei such as Al_nO_m or Ti_nO_m (e.g., Gail, 2003), whose formation is still not

well-understood. In carbonaceous grains, such as graphite and SiC, tiny sub-crystals of highly refractory carbides (TiC or (Zr,Ti,Mo)C) have been detected, which similarly indicate seed nucleation processes before condensation of the major phase (Bernatowicz et al., 1996; Croat et al., 2003). However, the first TEM analyses on presolar silicates did not identify such tiny sub-crystals (Messenger et al., 2003; Floss et al., 2006; Nguyen et al., 2007b; Vollmer et al., 2007a,b; Yada et al., 2008). Ca–Al-rich minerals such as corundum, hibonite, grossite, spinel or mellite are expected to condense from a gas of solar composition before the major silicates forsterite and enstatite form (e.g., Lodders, 2003). Highly refractory grains of solar system origin such as corundum aggregates or corundum overgrown by hibonite have been found in the carbonaceous chondrite Acfer 094 (Nakamura et al., 2007). These grains have been explained by condensation of pure corundum from the cooling solar gas and subsequent, diffusion-controlled formation of hibonite by reaction with gaseous Ca. Such grains can then serve as seed nuclei onto which lower temperature silicates accrete. This implies that the composition of the gas changes during formation and that the condensing grain and the cooling gas are not in chemical equilibrium, because forming grains are removed kinetically. A similar process could also be imagined for grain 7_04 and the series of grains in 22_09, which are indeed best-explained by a condensation sequence (Figs. 8 and 9). The higher-temperature Al-rich oxide (corundum, hibonite or grossite) forms first followed by the Ca–Si-rich phase and the Fe-bearing silicate condensing at progressively lower temperatures. It is an interesting observation that the silicates in both complex grains with acquired Auger data (22_09 and 32_03) are Si-enriched and clearly did not form under equilibrium conditions. This is consistent with the proposed non-equilibrium formation process for these types of grains, where forming phases are removed kinetically and cannot react with the gas anymore. The overall O-isotopic composition of the gas remained constant during this sequence, at least within the errors of our analyses. Theoretically, these composite grains are predicted to be dependent on different stellar mass-loss rates, which also influence silicate crystallinity (Sogawa and Koza-sa, 1999). However, in our case the accreted silicate has a non-stoichiometric composition and is, therefore, probably not crystalline. From an observational point of view this dependence on the mass-loss rate is also expected. In fact, the detection of Al-rich refractory oxides in IR spectra depends on the mass-loss rate, and at higher mass-loss rates refractory oxides are not observed anymore, likely being coated by silicate mantles (Dijkstra et al., 2005). In this study, only grain 7_04 is completely coated, but the other two complex grains could represent fragments of former intact, larger assemblages. The heterogeneity of grain 32_03 on a fine scale (Fig. 10) argues for a rather complex formation process, as Al-rich phases and silicates seem to have condensed in no specific order. This is different from the other two grains, where the phases seem to have accreted successively.

It is noteworthy, that the number of complex grains is small compared to the majority of presolar silicates without recognizable refractory seed nuclei. If these complex grains

support theories of heterogeneous silicate nucleation, it is unclear why the majority of silicate grains condensed homogeneously without such subgrains. One possible explanation is that subgrains are present but might have been overlooked, except in the case of the complex grains, which are the largest members of this population. This could be due to the grain orientation in the polished section, where a two-dimensional image can only give an incomplete representation of a three-dimensional object. The chemically complex nature of most presolar silicates analyzed by TEM also makes it very difficult to distinguish Ca- or Al-rich subgrains from the surrounding silicate because the compositional contrast difference is very weak. Bulk EDX analyses by TEM on presolar silicates indeed show the presence of refractory elements like Al and Ca in some cases, as do Auger Nanoprobe analyses, although, as noted earlier, much of the Ca present in our grains may be due to secondary contamination. Therefore, it is possible that some silicates indeed condensed heterogeneously, but that seed clusters are too tiny to be identified. Second, although thermodynamically unfavorable, it is possible that silicate grains do condense homogeneously. This process depends heavily on the vapor pressure of gaseous Si–O, which could nucleate at higher temperatures than previously thought from a super-saturated gas (Nuth and Ferguson, 2006). More experimental and theoretical work is necessary to explore the homogeneous growth of silicates. Third, it is possible that a higher fraction of the presolar silicate inventory could originally have formed as complex grains, but was shattered by interstellar shock waves during ISM passage. Fragmentation due to grain–grain collisions in SN accelerated shock waves is an important modification process affecting interstellar dust grains (Jones et al., 1996). This process shifts the size distribution of the interstellar dust inventory to smaller values leaving the total dust mass unaltered. Therefore, what we find today as presolar grains could be the remainders of former complex grains that were fragmented into Al-rich oxides such as corundum and hibonite (Nittler et al., 1997; Choi et al., 1999) and silicates from former mantles. A tiny fraction of this material might undergo high-pressure modification, a process which has been proposed theoretically (Tielens et al., 1994) and was confirmed recently for a presolar silicate with a perovskite structure (Vollmer et al., 2007b). This latter possibility of fragmentation in the ISM might provide an explanation for the under-abundance of refractory subgrains in the presolar silicate population.

5. CONCLUSIONS

We have detected 138 presolar silicate, 20 presolar oxide and three presolar complex grains in the carbonaceous chondrite Acfer 094 by NanoSIMS oxygen isotope mapping. The majority of these grains were documented by FE-SEM for further morphological details and to investigate the distribution of presolar material within the meteorite matrix. We also analyzed 69 grains with Auger electron spectroscopy for their elemental compositions (30 on a quantitative, 39 on a qualitative basis). Our investigations lead us to the following conclusions:

- (1) Refractory Al-rich oxides may serve as seed nuclei for silicate material to condense, which is proposed by condensation theory as well as by observation of silicate-coated Al-rich oxides. However, the majority of presolar silicates apparently do not enclose large subgrains.
- (2) The majority of presolar silicates and oxides ($81 \pm 7\%$) in Acfer 094 belong to the O isotope Group I and come from low-mass AGB stars of close-to-solar or slightly lower-than-solar metallicity. Sixty percent of these grains are irregular in shape, 40% display an elliptical or circular morphology. Both grain morphologies are consistent with expectations from condensation experiments, but the irregular grains are more likely to have been altered by secondary processing. It is therefore possible that these different grain populations experienced different degrees of secondary alteration.
- (3) A fraction of presolar silicates and oxides are highly ^{17}O -enriched ($^{17}\text{O}/^{16}\text{O} > 3 \times 10^{-3}$) and might share a binary star (Nittler et al., 2008; Vollmer et al., 2008) or a $\sim 3 M_{\odot}$ AGB star origin. These grains have small sizes (generally < 250 nm) and highly irregular appearances, which might support theories that these grains did not form under standard conditions around low-mass AGB stars.
- (4) $11 \pm 3\%$ of the presolar silicates can be assigned to Group IV characterized by enrichments in ^{18}O relative to solar and close-to-solar $^{17}\text{O}/^{16}\text{O}$. These grains most probably derive from SNII explosions (Nittler et al., 2008; Vollmer et al., 2008). They are predominantly smaller and irregularly shaped consistent with the shorter condensation timescales of a SNII scenario.
- (5) The grains are evenly distributed within the matrix on an mm scale, but the clustering in one field containing five grains is statistically significant. This clustering might be the result of an extremely heterogeneous distribution of stardust in the solar nebula, which could have been inherited from the parental molecular cloud.
- (6) The matrix-normalized abundance of silicate stardust in Acfer 094 is 163 ± 14 ppm, and that of oxide stardust is 26 ± 6 ppm. The overall abundance of O-rich stardust in the nascent solar nebula may be close to this value, as abundances are similar in certain primitive CR3 chondrites and IDPs.
- (7) Auger measurements indicate that the majority of the presolar silicate grains are Fe-rich (Mg# of 0.82 and lower), which is either due to non-equilibrium condensation, secondary alteration or both.
- (8) (Mg + Fe)/Si ratios in most of the presolar silicates from this study are predominantly characterized by pyroxene- rather than olivine-like compositions, which is consistent with recent Auger and TEM analyses on a similar set of grains.
- (9) Mg-rich grains (Mg/(Mg + Fe) > 0.5) tend to exhibit elliptical, smooth surfaces (14 out of 18 grains), suggesting that these grains have not been strongly altered since their circumstellar condensation.
- (10) Some grains have (Mg + Fe)/Si ratios not compatible with either pyroxene or olivine indicating non-equilibrium condensation conditions. Only one GEMS-like grain similar to those usually found in IDPs (i.e., with a sulfur content $> 2\text{--}3$ at.%) has been identified among our population; this is consistent with results from recent Auger and TEM analyses. The reason for the low abundance of typical GEMS grains in primitive meteorites compared to IDPs remains unclear.

ACKNOWLEDGMENTS

We thank Franz Brandstätter for the loan of the meteorite thin section, Elmar Gröner for technical assistance on the NanoSIMS and Joachim Huth for his support at the SEM. We appreciate constructive and helpful reviews by Maria Lugaro, Larry Nittler and an anonymous reviewer as well as editorial handling and comments by the Associate Editor Trevor Ireland. A portion of this work was supported by NASA Grants NNX07AI82G (PI: C. Floss) and NNX08AI13G (PI: F. Stadermann).

REFERENCES

- Alexander C. M. O'. D. (2005) Re-examining the role of chondrules in producing the elemental fractionations in chondrites. *Meteorit. Planet. Sci.* **40**(7), 943–965.
- Alexander C. M. O'. D., Fogel M., Yabuta H. and Cody G. D. (2007) The origin and evolution of chondrites recorded in the elemental and isotopic compositions of their macromolecular organic matter. *Geochim. Cosmochim. Acta* **71**, 4380–4403.
- Bernatowicz T. J., Cowsik R., Gibbons P. C., Lodders K., Fegley, B., Amari S. and Lewis R. S. (1996) Constraints on stellar grain formation from presolar graphite in the Murchison meteorite. *Astrophys. J.* **472**, 760–782.
- Bland P. A., Howard K. T., Cressey G. and Benedix G. K. (2008) The terrestrial component of primitive chondrite alteration. *Meteorit. Planet. Sci.* **71**, A5314.
- Bland P. A., Stadermann F. J., Floss C., Rost D., Vicenzi E., Kearsley A. T. and Benedix G. (2007) A cornucopia of presolar and early solar system materials at the micrometer size range in primitive chondrite matrix. *Meteorit. Planet. Sci.* **42**, 1417–1427.
- Boctor N. Z., Kurat G. and Alexander C. M. O'. D. (2003) Sulfide-oxide assemblage in Tagish Lake carbonaceous chondrite. *Lunar Planet. Sci.* **34**, 1705.
- Boothroyd A. I. and Sackmann I.-J. (1999) The CNO isotopes: deep circulation in red giants and first and second dredge-up. *Astrophys. J.* **510**, 232–250.
- Bose M., Floss C. and Stadermann F. J. (2008a) Iron-enriched Stardust Grains in the Meteorites Acfer 094, QUE 99177 and MET 00426. *Meteorit. Planet. Sci.* **71**, A5094.
- Bose M., Stadermann F. J. and Floss C. (2008b) An investigation into the origin of Group 4 stardust grains. *Lunar Planet. Sci.* **39**, 1099.
- Bose M., Floss C. and Stadermann F. J. (2009) Presolar silicate and oxide dust in ALHA 77307. *Meteorit. Planet. Sci.* **72**, A5341.
- Bradley J. P. (1994) Chemically anomalous, preaccretionally irradiated grains in interplanetary dust from comets. *Science* **265**(5174), 925–929.
- Bradley J. P. (2003) The astromineralogy of interplanetary dust particles. In *Astromineralogy* (ed. Th. Henning), pp. 217–235.

- Bradley J. P. and Dai Z. R. (2004) Mechanism of formation of glass with embedded metal and sulfides. *Astrophys. J.* **617**, 650–655.
- Bradley J. P., Keller L. P., Snow T. P., Hanner M. S., Flynn G. J., Gezo J. C., Clemett S. J., Brownlee D. E. and Bowey J. E. (1999) An infrared spectral match between GEMS and interstellar grains. *Science* **285**, 1716–1718.
- Choi B.-G., Huss G. R., Wasserburg G. J. and Gallino R. (1998) Presolar corundum and spinel in ordinary chondrites: origins from AGB stars and a supernova. *Science* **282**, 1284–1289.
- Choi B.-G., Wasserburg G. J. and Huss G. R. (1999) Circumstellar hibonite and corundum and nucleosynthesis in asymptotic giant branch stars. *Astrophys. J.* **522**, L133–L136.
- Colangeli L., Henning T., Brucato J. R., Clément D., Fabian D., Guillois O., Huisken F., Jäger C., Jessberger E. K., Jones A., Ledoux G., Manicó G., Mennella V., Molster F. J., Mutschke H., Pirronello V., Reynaud C., Roser J., Vidali G. and Waters L. B. F. M. (2003) The role of laboratory experiments in the characterization of silicon-based cosmic material. *Astron. Astrophys. Rev.* **11**, 97–152.
- Croat T. K., Bernatowicz T. J., Amari S., Messenger S. and Stadermann F. J. (2003) Structural, chemical and isotopic microanalytical investigations of graphite from supernovae. *Geochim. Cosmochim. Acta* **67**(24), 4705–4725.
- Demyk K., Carrez P., Leroux H., Cordier P., Jones A., Borg J., Quirico E., Raynal P. I. and d'Hendecourt L. (2001) Structural and chemical alteration of crystalline olivine under low energy He⁺ irradiation. *Astron. Astrophys.* **368**, L38–L41.
- Dijkstra C., Speck A. K., Reid R. B. and Abraham P. (2005) The 10 μm feature of M-type stars in the large magellanic cloud and the dust condensation sequence. *Astrophys. J.* **633**, L133–L136.
- Ebata S., Fagan T. J. and Yurimoto H. (2007) Identification of silicate and carbonaceous presolar grains in the Type 3 enstatite chondrite ALHA81189. *Meteorit. Planet. Sci.* **70**, A5150.
- Fabian D., Henning T., Jäger C., Mutschke H., Dorschner J. and Wehrhan O. (2001) Steps toward interstellar silicate mineralogy: VI. Dependence of crystalline olivine IR spectra on iron content and particle shape. *Astron. Astrophys.* **378**, 228–238.
- Ferrarotti A. S. and Gail H.-P. (2001) Mineral formation in stellar winds: II. Effects of Mg/Si abundance variations on dust composition in AGB stars. *Astron. Astrophys.* **371**, 133–151.
- Floss C., Stadermann F. J., Bradley J. P., Dai Z. R., Bajt S., Graham G. and Lea A. S. (2006) Identification of isotopically primitive interplanetary dust particles: a NanoSIMS isotopic imaging study. *Geochim. Cosmochim. Acta* **70**, 2371–2399.
- Floss C., Stadermann F. J., Mertz A. F. and Bernatowicz T. J. (2007) Anatomy of an isotopically primitive interplanetary dust particle: coordinated NanoSIMS and Auger Nanoprobe analyses. *Lunar Planet. Sci.* **38**, 1145.
- Floss C., Stadermann F. J. and Bose M. (2008) Circumstellar Fe oxide from the Acfer 094 carbonaceous chondrite. *Astrophys. J.* **672**, 1266–1271.
- Floss C. and Stadermann F. J. (2009) Auger Nanoprobe analysis of presolar ferromagnesian silicate grains from primitive CR chondrites QUE 99177 and MET 00426. *Geochim. Cosmochim. Acta* **73**, 2415–2440.
- Floss C., Stadermann F. J., Yada T., Noguchi T. and Nakamura T. (2009) Anomalous nitrogen isotopic composition in the stardust-rich antarctic micrometeorite T98G8: affinities to primitive CR chondrites and anhydrous IDPs. *Lunar Planet. Sci.* **40**, 1082.
- Gail H.-P. (2003) Formation and evolution of minerals in accretion disks and stellar outflows. In *Astromineralogy* (ed. Th. Henning), pp. 55–120.
- Gail H.-P. and Sedlmayr E. (1999) Mineral formation in stellar winds: I. Condensation sequence of silicate and iron grains in stationary oxygen rich outflows. *Astron. Astrophys.* **347**, 594–616.
- Gail H.-P., Zhukovska S., Hoppe P. and Trieloff M. (2009) Stardust from asymptotic giant branch stars. *Astrophys. J.* **698**, 1136–1154.
- Greshake A. (1997) The primitive matrix components of the unique carbonaceous chondrite Acfer 094: a TEM study. *Geochim. Cosmochim. Acta* **61**(2), 437–452.
- Harris M. J. and Lambert D. L. (1984) Oxygen isotopic abundances in the atmospheres of seven red giant stars. *Astrophys. J.* **285**, 674–682.
- Hezel D. C., Palme H., Nasdala L. and Brenker F. E. (2006) Origin of SiO₂-rich components in ordinary chondrites. *Geochim. Cosmochim. Acta* **70**(6), 1548–1564.
- Hoppe P. and Vollmer C. (2008) Presolar silicates in meteorites and interplanetary dust particles. In *IXth Torino Workshop on Evolution and Nucleosynthesis in AGB Stars and the IInd Perugia Workshop on Nuclear Astrophysics. AIP Conference Proceedings*, vol. 1001, pp. 254–261.
- Jones A. P., Tielens A. G. G. M. and Hollenbach D. J. (1996) Grain shattering in shocks: the interstellar grain size distribution. *Astrophys. J.* **469**, 740–764.
- José J. and Hernanz M. (2007) The origin of presolar nova grains. *Meteorit. Planet. Sci.* **42**(7/8), 1135–1143.
- Keller L. P. and Messenger S. (2008) Coordinated chemical and isotopic studies of GEMS grains in IDPs. *Lunar Planet. Sci.* **39**, 2347.
- Keller L. P., Messenger S. and Christoffersen R. (2005) GEMS revealed: spectrum imaging of aggregate grains in interplanetary dust. *Lunar Planet. Sci.* **36**, 2088.
- Kemper F., de Koter A., Waters L. B. F. M., Bouwman J. and Tielens A. G. G. M. (2002) Dust and the spectral energy distribution of the OH/IR star OH 127.8+0.0: evidence for circumstellar metallic iron. *Astron. Astrophys.* **384**, 585–593.
- Kemper F., Vriend W. J. and Tielens A. G. G. M. (2004) The absence of crystalline silicates in the diffuse interstellar medium. *Astrophys. J.* **609**, 826–837.
- Leitner J., Hoppe P. and Zipfel J. (2009) NanoSIMS investigation of presolar silicates and oxides in primitive solar system materials. *Lunar Planet. Sci.* **40**, 1512.
- Lodders K. (2003) Solar system abundances and condensation temperatures of the elements. *Astrophys. J.* **591**, 1220–1247.
- Lugaro M., Karakas A. I., Nittler L. R., Alexander C. M. O' D., Hoppe P., Iliadis C. and Lattanzio J. C. (2007) On the asymptotic giant branch star origin of peculiar spinel grain OC2. *Astron. Astrophys.* **461**, 657–664.
- Maldoni M. M., Ireland T. R. and Robinson G. (2008) IRAS 22036+5306: an Al₂O₃ oxide-dominated post-AGB star. *Mon. Not. R. Astron. Soc.* **386**, 2290–2296.
- Marhas K. K., Hoppe P., Stadermann F. J., Floss C. and Lea A. S. (2006) The distribution of presolar grains in CI and CO meteorites. *Lunar Planet. Sci.* **37**, 1959.
- Messenger S., Keller L. P. and Lauretta D. S. (2005) Supernova olivine from cometary dust. *Science* **309**, 737–741.
- Messenger S., Keller L. P., Stadermann F. J., Walker R. M. and Zinner E. (2003) Samples of stars beyond the solar system: silicate grains in interplanetary dust. *Science* **300**, 105–108.
- Min M., Waters L. B. F. M., de Koter A., Hovenier J. W., Keller L. P. and Markwick-Kemper F. (2007) The shape and composition of interstellar silicate grains. *Astron. Astrophys.* **462**(2), 667–676.
- Molster F. J. and Kemper C. (2005) Crystalline silicates. *Space Sci. Rev.* **119**, 3–28.
- Molster F. J., Waters L. B. F. M. and Tielens A. G. G. M. (2002a) Crystalline silicate dust around evolved stars: II. The crystalline silicate complexes. *Astron. Astrophys.* **382**, 222–240.

- Molster F. J., Waters L. B. F. M., Tielens A. G. G. M. and Barlow M. J. (2002b) Crystalline silicate dust around evolved stars: I. The sample stars. *Astron. Astrophys.* **382**, 184–221.
- Molster F. J., Waters L. B. F. M., Tielens A. G. G. M., Koike C. and Chihara H. (2002c) Crystalline silicate dust around evolved stars: III. A correlations study of crystalline silicate features. *Astron. Astrophys.* **382**, 241–255.
- Mostefaoui S. and Hoppe P. (2004) Discovery of abundant in situ silicate and spinel grains from red giant stars in a primitive meteorite. *Astrophys. J.* **613**, L149–L152.
- Mostefaoui S., Marhas K. K. and Hoppe P. (2004) Discovery of an in-situ presolar silicate grain with GEMS-like composition in the Bishunpur matrix. *Lunar Planet. Sci.* **35**, 1593.
- Nagahara H. and Ozawa K. (2008) Heterogeneous nucleation and growth of metal on silicates and its astrophysical implication. *Lunar Planet. Sci.* **39**, 1241.
- Nakamura T. M., Sugiura N., Kimura M., Miyazaki A. and Krot A. N. (2007) Condensation and aggregation of solar corundum and corundum–hibonite grains. *Meteorit. Planet. Sci.* **42**(7/8), 1249–1265.
- Newton J., Bischoff A., Arden J. W., Franchi I. A., Geiger T., Greshake A. and Pillinger C. T. (1995) Acfer 094, a uniquely primitive carbonaceous chondrite from the Sahara. *Meteoritics* **30**, 47–56.
- Nguyen A. N. and Zinner E. (2004) Discovery of ancient silicate stardust in a meteorite. *Science* **303**, 1496–1499.
- Nguyen A., Busemann H. and Nittler L. R. (2007a) Remarkably high abundance of presolar grains in interplanetary dust particles collected from the comet Grigg-Skjellerup dust stream. *Lunar Planet. Sci.* **38**, 2332.
- Nguyen A., Stadermann F. J., Zinner E., Stroud R. M., Alexander C. M. O' D. and Nittler L. R. (2007b) Characterization of presolar silicate and oxide grains in primitive carbonaceous chondrites. *Astrophys. J.* **656**, 1223–1240.
- Nguyen A., Alexander C. M. O' D. and Nittler L. R. (2008a) An abundant mix of presolar matter in the highly primitive CR chondrite QUE 99177. *Meteorit. Planet. Sci.* **71**, A5277.
- Nguyen A., Stadermann F. J., Nittler L. R. and Alexander C. M. O' D. (2008b) Characterization of presolar silicate and oxide grains using Nanosims and Auger Spectroscopy. *Lunar Planet. Sci.* **39**, 2142.
- Nittler L. R. (2007) Presolar grain evidence for low-mass supernova injection into the solar nebula. In *Workshop on the Chronology of Meteorites and the Early Solar System, Kauai*, LPI Contribution No. **1374**, pp. 125–126.
- Nittler L. R., Alexander C. M. O' D., Gao X., Walker R. M. and Zinner E. (1997) Stellar sapphires: the properties and origins of presolar Al₂O₃ in meteorites. *Astrophys. J.* **483**, 475–495.
- Nittler L. R., Alexander C. M. O' D., Gallino R., Hoppe P., Nguyen A. N., Stadermann F. J. and Zinner E. (2008) Aluminum-, calcium- and titanium-rich oxide stardust in ordinary chondrite meteorites. *Astrophys. J.* **682**, 1450–1478.
- Nollett K. M., Busso M. and Wasserburg G. J. (2003) Cool bottom processes on the thermally pulsing asymptotic giant branch and the isotopic composition of circumstellar dust grains. *Astrophys. J.* **582**, 1036–1058.
- Nuth J. A. and Ferguson F. T. (2006) Silicates do nucleate in oxygen-rich circumstellar outflows: new vapor pressure data for SiO. *Astrophys. J.* **649**, 1178–1183.
- Posch T., Mutschke H., Trieloff M. and Henning T. (2007) Infrared spectroscopy of calcium–aluminium-rich inclusions: analog material for protoplanetary dust? *Astrophys. J.* **656**, 615–620.
- Rho J., Kozasa T., Reach W. T., Smith J. D., Rudnick L., DeLaney T., Ennis J. A., Gomez H. and Tappe A. (2008) Freshly formed dust in the Cassiopeia A Supernova remnant as revealed by the Spitzer Space Telescope. *Astrophys. J.* **673**, 271–282.
- Rietmeijer F. J. M., Nuth J. A., Karner J. M. and Hallenbeck S. L. (2002) Gas-to-solid condensation in a Mg–SiO–H₂–O₂ vapor: metastable eutectics in the MgO–SiO₂ phase diagram. *Phys. Chem. Chem. Phys.* **4**, 546–551.
- Sargent B. A., Forrest W. J., Tayrien C., McClure M. K., Li A., Basu A. R., Manoj P., Watson D. M., Bohac C. J., Furlan E., Kim K. H., Green J. D. and Sloan G. C. (2009) Silica in protoplanetary disks. *Astrophys. J.* **690**, 1193–1207.
- Scott E. R. D. and Krot A. N. (2003) Chondrites and their components. In *Treatise on Geochemistry* (eds. A. M. Davis, H. D. Holland and K. K. Turekian), pp. 143–200.
- Sogawa H. and Kozasa T. (1999) On the origin of crystalline silicate in circumstellar envelopes of oxygen-rich asymptotic giant branch stars. *Astrophys. J.* **516**, L33–L36.
- Stadermann F. J., Floss C., Bose M. and Lea A. S. (2009) The use of Auger spectroscopy for the in situ elemental characterization of sub-micrometer presolar grains. *Meteorit. Planet. Sci.*, in press.
- Stroud R. M., Nguyen A., Alexander C. M. O' D., Nittler L. R. and Stadermann F. J. (2008) Transmission electron microscopy of in situ presolar silicates in Alan Hills 77307. *Meteorit. Planet. Sci.* **71**, A5201.
- Tagigawa A., Tachibana S. and Nagahara H. (2008) Effects of anisotropic evaporation of circumstellar forsterite on infrared spectra. *Lunar Planet. Sci.* **39**, 1523.
- Tielens A. G. G. M., McKee C. F., Seab C. G. and Hollenbach D. J. (1994) The physics of grain–grain collisions and gas–grain sputtering in interstellar shocks. *Astrophys. J.* **431**, 321–340.
- Tonotani A., Kobayashi S., Nagashima K., Sakamoto N., Russell S. S., Itoh S. and Yurimoto H. (2006) Presolar grains from primitive ordinary chondrites. *Lunar Planet. Sci.* **37**, 1539.
- Vollmer C., Hoppe P., Brenker F. E. and Palme H. (2006) A complex presolar grain in Acfer 094—fingerprints of a circumstellar condensation sequence? *Lunar Planet. Sci.* **37**, 1284.
- Vollmer C., Hoppe P., Brenker F. E. and Holzapfel C. (2007a) A presolar silicate trilogy: condensation, coagulation, transformation—new insights from NanoSIMS/TEM investigations. *Lunar Planet. Sci.* **38**, 1262.
- Vollmer C., Hoppe P., Brenker F. E. and Holzapfel C. (2007b) Stellar MgSiO₃ perovskite: a shock-transformed stardust silicate found in a meteorite. *Astrophys. J.* **666**, L49–L52.
- Vollmer C., Hoppe P. and Brenker F. E. (2008) Si isotopic compositions of presolar silicate grains from red giant stars and supernovae. *Astrophys. J.* **684**, 611–617.
- Vollmer C., Brenker F. E., Hoppe P. and Stroud R. M. (2009) Direct laboratory analysis of silicate stardust from red giant stars. *Astrophys. J.* **700**, 774–782.
- Yada T., Floss C., Stadermann F. J., Zinner E., Nakamura T., Noguchi T. and Lea A. S. (2008) Stardust in antarctic micrometeorites. *Meteorit. Planet. Sci.* **43**(8), 1287–1298.
- Zhukovska S., Gail H.-P. and Trieloff M. (2008) Evolution of interstellar dust and stardust in the solar neighbourhood. *Astron. Astrophys.* **479**(2), 453–480.